



HAL
open science

Mitochondria-targeted hydroxyurea inhibits OXPHOS and induces antiproliferative and immunomodulatory effects

Gang Cheng, Micael Hardy, Paytsar Topchyan, Ryan Zander, Peter Volberding, Weiguo Cui, Balaraman Kalyanaraman

► **To cite this version:**

Gang Cheng, Micael Hardy, Paytsar Topchyan, Ryan Zander, Peter Volberding, et al.. Mitochondria-targeted hydroxyurea inhibits OXPHOS and induces antiproliferative and immunomodulatory effects. *iScience*, 2021, 10.1016/j.isci.2021.102673 . hal-03627839

HAL Id: hal-03627839

<https://amu.hal.science/hal-03627839v1>

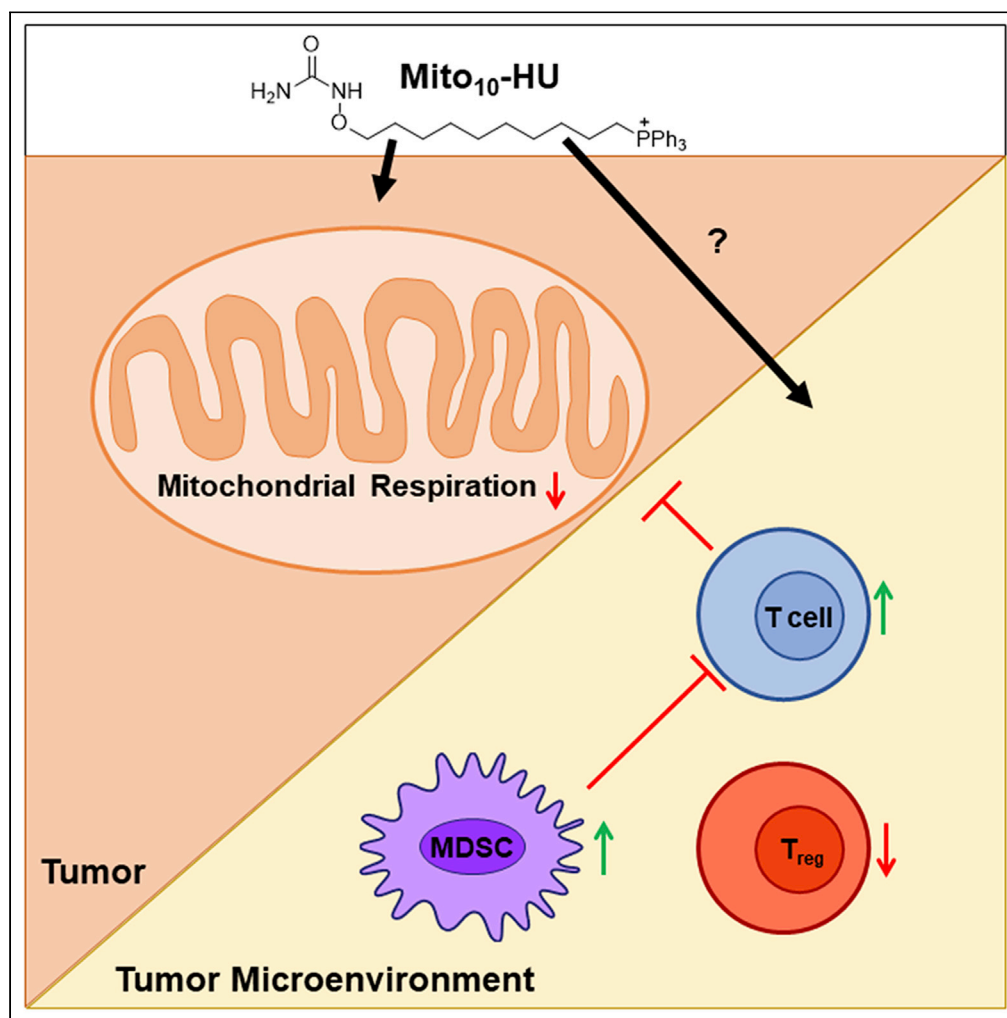
Submitted on 1 Apr 2022

HAL is a multi-disciplinary open access archive for the deposit and dissemination of scientific research documents, whether they are published or not. The documents may come from teaching and research institutions in France or abroad, or from public or private research centers.

L'archive ouverte pluridisciplinaire **HAL**, est destinée au dépôt et à la diffusion de documents scientifiques de niveau recherche, publiés ou non, émanant des établissements d'enseignement et de recherche français ou étrangers, des laboratoires publics ou privés.

Article

Mitochondria-targeted hydroxyurea inhibits OXPHOS and induces antiproliferative and immunomodulatory effects



Gang Cheng,
Micael Hardy,
Paytsar Topchyan,
Ryan Zander,
Peter Volberding,
Weiguo Cui,
Balaraman
Kalyanaraman

balarama@mcw.edu

Highlights

Mito-HUs target OXPHOS & inhibit cancer cell proliferation at sub-micromolar levels

More hydrophobic Mito-HUs more potently inhibit mitochondrial respiration

More hydrophobic Mito-HUs may inhibit MDSCs & neutrophils, activate T cells

The IC₅₀s for inhibition are similar in tumor cells, MDSCs, and neutrophils

Cheng et al., iScience 24, 102673
June 25, 2021 © 2021 The Authors.
<https://doi.org/10.1016/j.isci.2021.102673>

Article

Mitochondria-targeted hydroxyurea inhibits OXPHOS and induces antiproliferative and immunomodulatory effects

Gang Cheng,^{1,2} Micael Hardy,⁶ Paytsar Topchyan,^{3,7} Ryan Zander,^{3,7} Peter Volberding,^{3,7} Weiguo Cui,^{3,7} and Balaraman Kalyanaraman^{1,2,4,5,8,*}

SUMMARY

Hydroxyurea (HU), an FDA-approved drug for treating sickle cell disease, is used as an antitumor drug alone and together with conventional chemotherapeutics or radiation therapy. HU is used primarily to treat myeloproliferative diseases because it inhibits the enzyme ribonucleotide reductase involved in DNA synthesis. The hydroxyl group in HU is considered critical for its antiproliferative and chemotherapeutic effects. Here, we substituted the hydroxyl group in HU with a triphenylphosphonium cation attached to an alkyl group with different chain lengths, forming a new class of mitochondria-targeted HU (Mito-HU). Elongating the alkyl side chain length increased the hydrophobicity of Mito-HUs, inhibition of oxidative phosphorylation, and antiproliferative effects in tumor cells. Both mitochondrial complex I- and complex III-induced oxygen consumption decreased with the increasing hydrophobicity of Mito-HUs. The more hydrophobic Mito-HUs also potently inhibited the monocytic myeloid-derived suppressor cells and suppressive neutrophils, and stimulated T cell response, implicating their potential antitumor immunomodulatory mechanism.

INTRODUCTION

Hydroxyurea (HU), also known as hydroxycarbamide (trade names Hydrea and Droxia), is a chemotherapeutic agent used to treat melanoma, refractory chronic myelocytic leukemia (CML), recurring and inoperable ovarian cancer, and squamous cell carcinoma of the head and neck (Spivak and Hasselbalch, 2011; Madaan et al., 2012; Singh and Xu, 2016; Grund et al., 1977). HU belongs to a group of chemotherapeutic agents known as “antimetabolites” that interfere with the production of nucleic acids (Koç et al., 2004; Singh and Xu, 2016). HU inhibits the multi-enzyme complex, ribonucleotide diphosphate reductase (RDR), an enzyme that catalyzes the conversion of ribonucleotide to deoxyribonucleotide during *de novo* DNA synthesis (Teng et al., 2018; Koç et al., 2004; Zhou et al., 2013). HU has been used in combination with other modalities, conventional chemotherapeutics, and radiation therapy. RDR also is involved in DNA repair. When combined with radiation, the therapeutic efficacy of HU is increased because it inhibits DNA repair (Teng et al., 2018; Madaan et al., 2012; Singh and Xu, 2016). In cancer patients, HU has been used extensively as a radiation sensitizer by synchronizing cells in a radiation-sensitive S-phase of the cell cycle (Yarbro, 1992). In addition, HU inhibits the repair of radiation-induced DNA damage (Singh and Xu, 2016). HU is blood-brain barrier permeable and, in combination with temozolomide, was used as an adjuvant therapy for glioblastoma patients (Teng et al., 2018).

Several decades ago, HU was shown to inhibit L1210 leukemia cells and various solid tumors (Mai et al., 2010; Ren et al., 2002). Later, HU was shown to be effective against myeloproliferative disorders, CML, and polycythemia rubra vera (Spivak and Hasselbalch, 2011). It was also postulated that HU could stimulate an immune response in melanoma and lung cancer by recruiting components of the innate immune system (Cheng et al., 2020b; Oo et al., 2019). Typically, high concentrations of HU are required for *in vitro* and *in vivo* efficacy in chemotherapy (Singh and Xu, 2016). The high dose of HU is attributed to its side effects and drug resistance (Madaan et al., 2012; Singh and Xu, 2016). HU (H₂N-CO-NHOH) is the hydroxylated analog of urea (NH₂-CO-NH₂). The hydroxyl group (OH in HU) is thought to be critical for its antiproliferative and antitumor mechanisms (Madaan et al., 2012; Singh and Xu, 2016). In this study, we modified the structure

¹Department of Biophysics, Medical College of Wisconsin, 8701 Watertown Plank Road, Milwaukee, WI 53226, USA

²Free Radical Research Center, Medical College of Wisconsin, 8701 Watertown Plank Road, Milwaukee, WI 53226, USA

³Microbiology & Immunology, Medical College of Wisconsin, 8701 Watertown Plank Road, Milwaukee, WI 53226, USA

⁴Cancer Center, Medical College of Wisconsin, 8701 Watertown Plank Road, Milwaukee, WI 53226, USA

⁵Center for Disease Prevention Research, Medical College of Wisconsin, 8701 Watertown Plank Road, Milwaukee, WI 53226, USA

⁶Aix Marseille Univ, CNRS, ICR, UMR 7273, Marseille 13013, France

⁷Versiti Blood Research Institute, 8733 Watertown Plank Road, Milwaukee, WI 53226, USA

⁸Lead contact

*Correspondence: balarama@mcw.edu

<https://doi.org/10.1016/j.isci.2021.102673>



of HU by replacing the -OH group with a triphenylphosphonium cation (TPP^+)-containing group. These modified HU derivatives inhibited mitochondrial oxygen consumption more potently than HU and are, therefore, designated as mitochondria-targeted HUs (Mito-HUs).

Increasing evidence suggests that certain subtypes of cancer cells, including cancer stem cells and chemotherapy-resistant cancer cells, utilize oxidative phosphorylation (OXPHOS) to obtain the energy needed for survival and proliferation (Fiorillo et al., 2016; Xu et al., 2020). Targeting OXPHOS, especially mitochondrial complex I, is emerging as a potential antitumor strategy to treat several types of cancer (Cheng et al., 2013, 2016, 2019; Boyle et al., 2018; Weinberg and Chandel, 2015; Xu et al., 2020; Fischer et al., 2019; Pan et al., 2018). As previously suggested (American Association for Cancer Research, 2019), OXPHOS inhibitors that target cancer cells will also target cancer-associated immune cells. Reports suggest that suppression of OXPHOS function in cancer cells could influence the tumor microenvironment (TME) by inhibiting hypoxia and enhancing the antitumor response (Xu et al., 2020). However, to our knowledge, mitochondria-targeted derivatives with varying hydrophobicities on cytotoxic and tumor suppressive cells in the TME have not been thoroughly tested. Reports indicate that cancer patients with enhanced myeloid-derived suppressor cells (MDSCs) and regulatory T cells (T_{regs}) have lower survival compared to patients with decreased MDSCs (Solito et al., 2011; Saleh and Elkord, 2020). Therefore, MDSCs and T_{regs} are promising targets for antitumor treatment (Kawano et al., 2015).

The chemotherapeutic agents (gemcitabine and 5-fluorouracil) currently used to inhibit MDSCs cause bone marrow suppression; clearly, less toxic and targeted agents are needed to inhibit MDSCs and/or suppressive neutrophils as well as to enhance the cytotoxic antitumor function of T cells (Sawant et al., 2013; Law et al., 2020; Hossain et al., 2015). MDSCs suppress T cells that destroy tumor cells (Nagaraj et al., 2013). Broadly designed MDSCs comprise both monocytic MDSCs (M-MDSC) and suppressive neutrophils. In this study, we investigated the antiproliferative and immunomodulatory effects of Mito-HUs with varying hydrophobicities. The results show that more hydrophobic Mito-HUs potently inhibit the proliferation of tumor cells, inhibit the differentiation of M-MDSCs and suppressor neutrophils, and stimulate the effector T cell (T_{eff}) response.

RESULTS

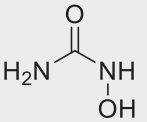
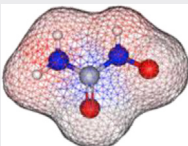
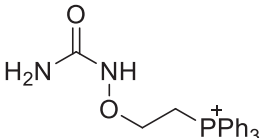
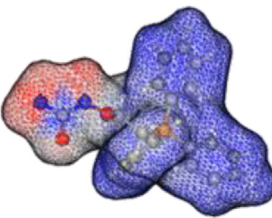
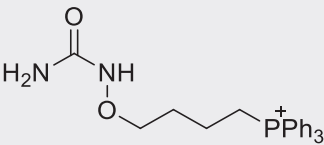
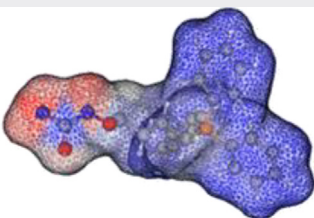
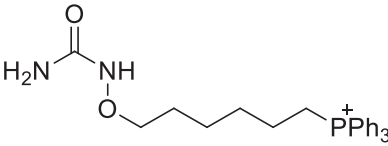
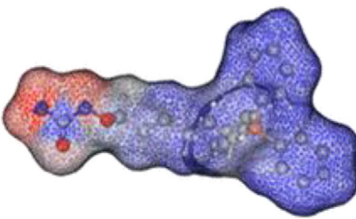
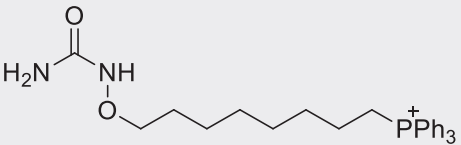
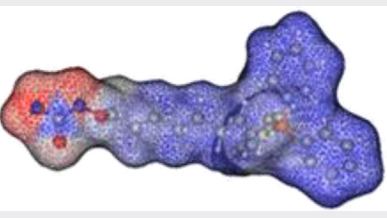
Substitution of the -OH group in HU with increasing alkyl side chain lengths increases the hydrophobicity in Mito-HUs

To assess the relative hydrophobicity of HU and Mito-HU derivatives, we calculated the octanol/water partition coefficients ($\log P$) using a QSAR (quantitative structure-activity relationships) analysis and rational drug design as a measure of molecular hydrophobicity (Table 1). This method also uses a consensus model built using the ChemAxon software (San Diego, CA) (Viswanadhan et al., 1989; Klopman et al., 1994). Table 1 lists the $\log p$ values along with the calculated regions of the relative hydrophilic and hydrophobic regions. HU is very polar, and the calculated $\log p$ value is -1.4 (Table 1). The calculated value agrees with the experimentally determined oil-to-water $\log p$ value (i.e., -1.8) for HU (Ren et al., 2002). The extreme water solubility of HU, necessitating the use of a high dosage and frequency of administration for therapeutic efficacy, resulted in the rapid development of drug resistance (Madaan et al., 2012; Singh and Xu, 2016). Thus, we surmised that increasing its hydrophobicity might enhance drug potency. Table 1 presents the structures of various Mito-HUs and controls as well as the calculated hydrophobicity (see supplemental information). Results shown below suggest that derivatization of the -OH group in HU with a TPP^+ -containing alkyl side chain enhances the antiproliferative efficacy, with increasing hydrophobicity.

Increased hydrophobicity associated with increased antiproliferative potency and decreased mitochondrial oxygen consumption

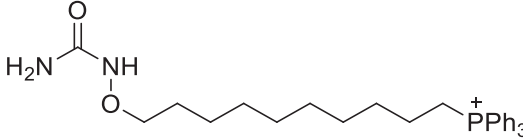

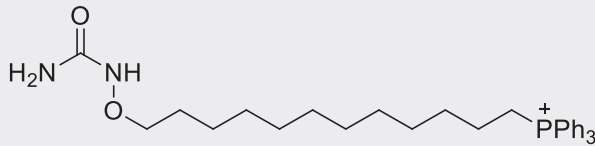
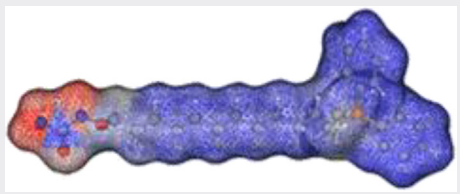
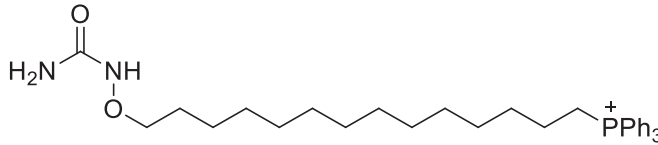
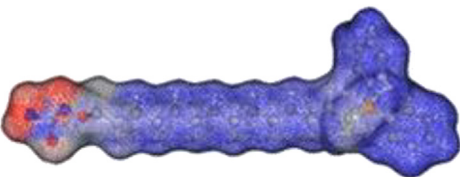
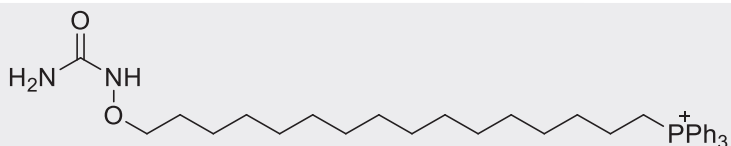

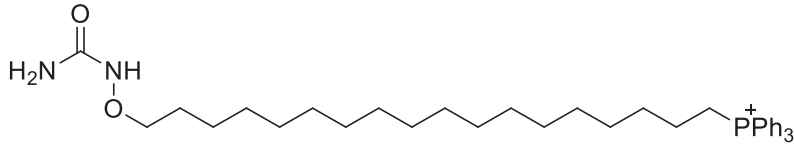
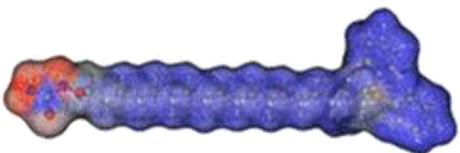
Cell proliferation was monitored continuously in an IncuCyte Live-Cell Analysis system (Cheng et al., 2013, 2016; Boyle et al., 2018) using HU and Mito-HUs (Mito₄-HU, Mito₁₀-HU, Mito₁₂-HU, Mito₁₄-HU, Mito₁₆-HU, and Mito₂₀-HU; Figure 1A). Mito₄-HU, Mito₁₀-HU, Mito₁₂-HU, Mito₁₄-HU, Mito₁₆-HU, and Mito₂₀-HU dose-dependently inhibited proliferation of HCT116 human colon cancer cells (Figures 1A and 1B). A Mito-HU with an alkyl chain length ≥ 10 is more potent than HU at inhibiting the proliferation of HCT116 cells. Figure 1B shows the cell confluence (indicated by a dotted line) as a function of Mito-HU concentration, and the half maximal inhibitory concentration (IC_{50} , μM) values of Mito₄-HU, Mito₁₀-HU, Mito₁₂-HU, Mito₁₄-HU, Mito₁₆-HU, and Mito₂₀-HU are >600 μM , 8.0 μM , 1.8 μM , 0.74 μM , 0.51 μM , and 0.23 μM , respectively (Table S1). As compared with Mito-HUs, HU inhibited cell proliferation at much higher concentrations (Figure 1B). These results suggest that enhancing the hydrophobicity by attaching a longer aliphatic chain containing a

Table 1. Calculated partition coefficients and relative hydrophobic regions in HU and Mito-HUs

Molecule	Structure	log P*	
Hydroxyurea (HU)		-1.4	
Mito ₂ -HU		3.3	
Mito ₄ -HU		4.0	
Mito ₆ -HU		4.9	
Mito ₈ -HU		5.8	

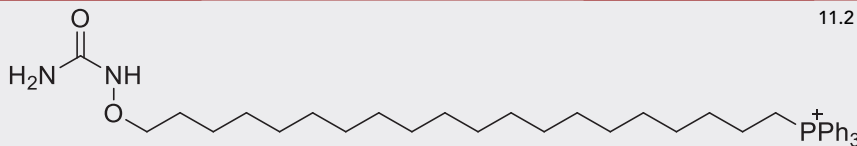
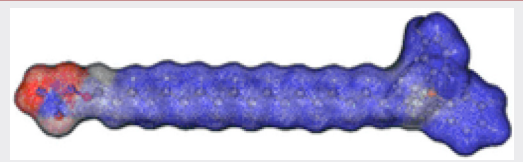
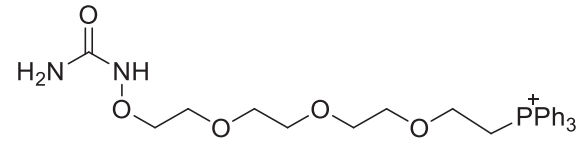
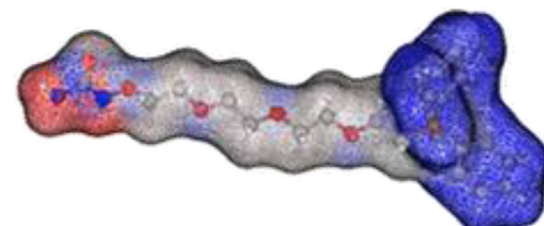
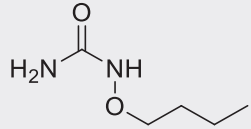
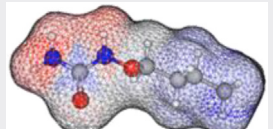
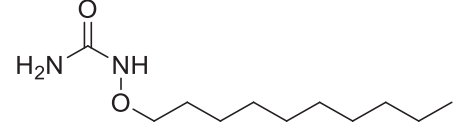
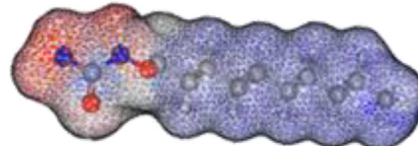
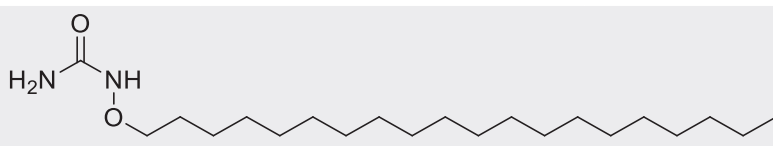

(Continued on next page)

Table 1. Continued

Molecule	Structure	log P*	
Mito ₁₀ -HU		6.7	
Mito ₁₂ -HU		7.6	
Mito ₁₄ -HU		8.5	
Mito ₁₆ -HU		9.4	
Mito ₁₈ -HU		10.3	

(Continued on next page)

Table 1. Continued

Molecule	Structure	log P*	
Mito ₂₀ -HU		11.2	
Mito-PEG-HU		3.1	
Butyl-HU		0.3	
Decyl-HU		3.0	
Eicosanyl-HU		7.5	

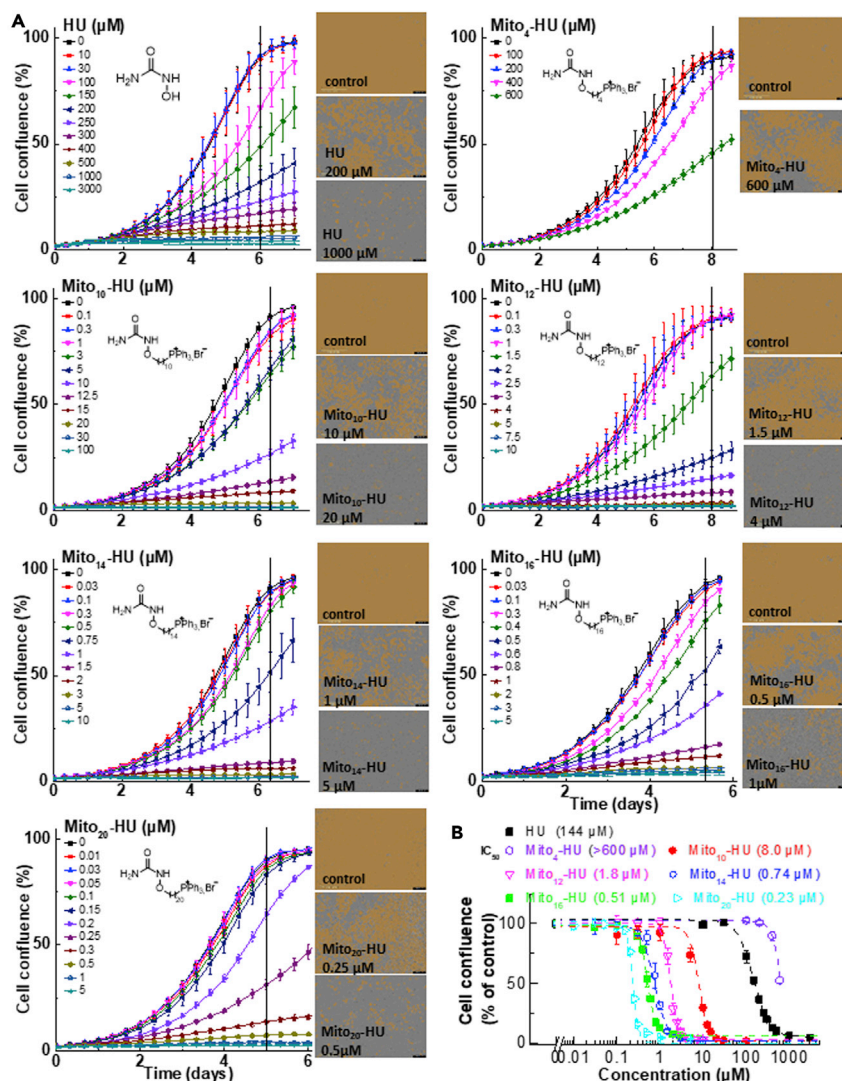


Figure 1. Effects of HU and Mito-HUs on proliferation of HCT116 human colon cancer cells

(A) Effects of HU and Mito-HUs on the proliferation of HCT116 cells were monitored in the IncuCyte Live-Cell Analysis system. The IncuCyte Analyzer provides real-time updates on cell confluence, based on segmentation of high definition-phase contrast images. Representative cell images were shown as segmentation mask illustrated in brown when control cells reached 90% confluence (vertical solid black line).

(B) The IC_{50} values were determined at the point at which control cells reached $\sim 90\%$ confluence (vertical solid black line). Relative cell confluence (control is taken as 100%) is plotted against concentration. Dashed lines represent the fitting curves used to determine the IC_{50} values as indicated. Data shown are the means \pm SD.

TPP⁺ group to HU greatly increases the antiproliferative potency. The antiproliferative effects of Mito₁₂-HU, Mito₁₄-HU, Mito₁₆-HU, and Mito₂₀-HU are ~ 100 – 600 times more potent than those of HU. In control experiments, we used compounds (decyl-HU) with an alkyl carbon-carbon side chain length similar to that of Mito₁₀-HU but lacking the TPP⁺. Decyl-HU ($\text{IC}_{50} > 600 \mu\text{M}$; Figure S1) was much less effective than the corresponding Mito₁₀-HU ($\text{IC}_{50} = 8.0 \mu\text{M}$; Figure 1B). Results obtained using decyl-HU confirm that the TPP⁺ moiety in Mito₁₀-HU is required to enhance its antiproliferative activity. The statistical analyses of results (Figure 1) are shown in Table S2.

We also tested the relative inhibitory effects of HU and Mito₁₀-HU on the proliferation of MiaPaCa-2 human pancreatic cancer cells (Figure S2). Mito₁₀-HU was nearly 100 times more potent than HU in inhibiting MiaPaCa-2 cell proliferation (Figure S2).

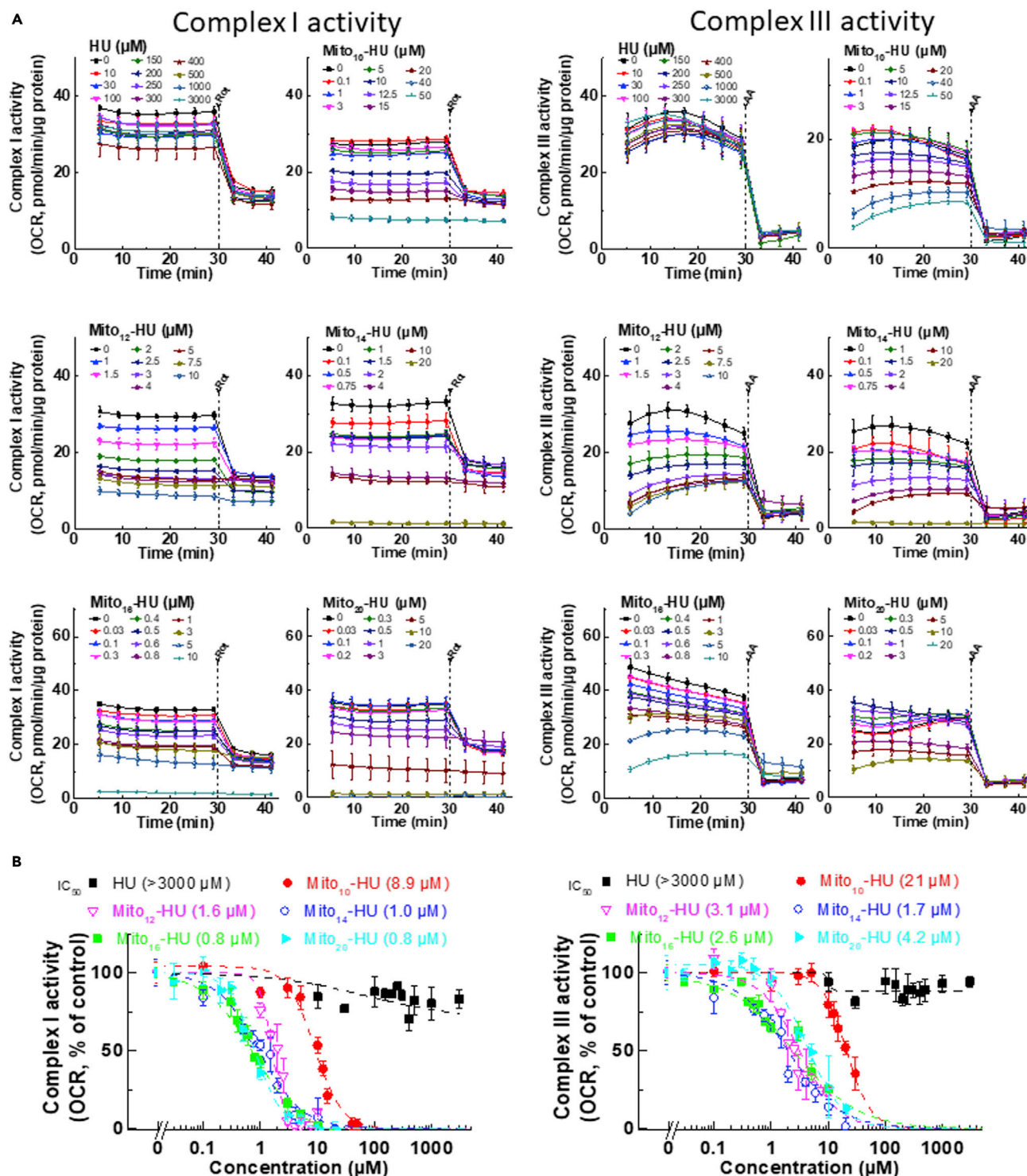


Figure 2. Effects of HU and Mito-HUs on the oxygen consumption by mitochondrial complexes I and III

(A) Dose-dependent effects of HU, Mito₁₀-HU, Mito₁₂-HU, Mito₁₄-HU, Mito₁₆-HU, and Mito₂₀-HU on complex I- and complex III-dependent oxygen consumption were measured in HCT116 cells. HCT116 cells were treated with HU or Mito-HUs as indicated for 24 hr. Mitochondrial complex I activity (left) and complex III activity (right) were monitored by a Seahorse XF-96 analyzer. Either rotenone (complex I inhibitor) or antimycin A (complex III inhibitor) was acutely added and OCR assayed immediately.

Figure 2. Continued

(B) The mitochondrial complex I (left) and III (right) dependent oxygen consumption (calculated as rotenone or antimycin A inhibitable OCR) are plotted against concentration of HU and Mito-HUs. Dashed lines represent the fitting curves used for determination of the IC_{50} values. Data shown are the means \pm SD.

Mito₁₀-HU_{NHTPP}⁺ (Figure S3) was designed and synthesized to compare the effects of O-alkylation and N-substitution on HU by the aliphatic chain containing a TPP⁺. Results also show that attaching a 10-carbon aliphatic chain containing a TPP⁺ group to the amino group of HU (as in Mito₁₀-HU_{NHTPP}⁺) inhibited HCT116 cell proliferation (Figure S3). This inhibition is similar to that of a 10-carbon aliphatic chain containing a TPP⁺ group to the ⁻OH group in HU (as in Mito₁₀-HU) (Figure S3). This result confirms that the antiproliferative effect of Mito₁₀-HU is not dependent on the free amino group.

Furthermore, we provided additional results in support of our hypothesis that enhancing the hydrophobicity of mitochondria-targeted TPP⁺ compounds (without increasing the chain length) increases their antiproliferative effects. We synthesized new compounds in which the phenyl groups in Mito₁₀-HU were substituted by three methyl groups (e.g., Mito-HU_{triMe}). The hydrophobicity of Mito₁₀-HU (log P = 6.7) is increased by the substitution of three methyl groups, Mito₁₀-HU_{triMe} (log P = 8.3). As shown in Figure S4, Mito₁₀-HU_{triMe} inhibited HCT116 cell proliferation at a lower concentration (IC_{50} = 3.7 μ M; log P = 8.3) than Mito₁₀-HU (IC_{50} = 8.0 μ M; log P = 6.7).

We used the SYTOX Green assay to monitor cell toxicity in an IncuCyte Live-Cell Analysis system. We tested the toxicity of Mito-HUs with varying hydrophobicities at their IC_{50} concentrations obtained from cell proliferation results (Figure 1B). A representative picture for Mito-HUs is shown in Figure S5. Although a 50% inhibition of cell proliferation was observed at this concentration (Figure 1 and Table S1), none of the Mito-HUs induced any apparent toxicity compared with control cells. These results suggest that the antiproliferative effects of Mito-HUs with varying side chain lengths are not due to nonspecific cellular toxicity. Permeabilization of cells with digitonin showed the total number of cells with or without Mito-HU treatments (Figure S5). Results revealed that the total number of cells was decreased in Mito-HU-treated cells, consistent with the increased antiproliferative effects of Mito-HUs with increased hydrophobicity.

Mitochondrial complex activities were assessed by measuring the oxygen consumption rate (OCR) using the Seahorse technique (Cheng et al., 2013, 2016, 2019; Boyle et al., 2018; Fiorillo et al., 2016). We tested the efficacy of Mito-HUs with varying alkyl side chain lengths on complex I- and complex III-induced oxygen consumption. HCT116 cells were treated with Mito-HUs at different concentrations for 24 hr, and the complex I- or complex III-induced OCR was measured. As shown in Figure 2A, Mito₁₀-HU effectively inhibited complex III-induced oxygen consumption and, more importantly, Mito₁₀-HU caused a significantly greater inhibition of mitochondrial complex I-driven oxygen consumption while HU had no apparent effects on either complex I- or complex III-driven oxygen consumptions. The IC_{50} values for Mito₁₀-HU to inhibit oxygen consumption by complex I and complex III are 8.9 μ M and 21 μ M, respectively (Figure 2B). Mito₁₀-HU, Mito₁₂-HU, Mito₁₄-HU, Mito₁₆-HU, and Mito₂₀-HU potently inhibited both mitochondrial complex I- and complex III-induced oxygen consumption in HCT116 cells (Figure 2B). For comparison, MiaPaCa-2 cells also were treated with Mito₁₀-HU at different concentrations for 24 hr, and the complex I- or complex III-induced oxygen consumption was measured. Mito₁₀-HU inhibited complex I- and complex III-induced oxygen consumption in MiaPaCa-2 cells (Figure S6); the IC_{50} values to inhibit complex I- and complex III-induced oxygen consumption are slightly lower than those reported for HCT116 cells. Furthermore, Mito₁₀-HU_{triMe} inhibited complex I- and complex III-induced oxygen consumption more potently than Mito₁₀-HU in HCT116 cells (Figure S7). This result is consistent with Mito₁₀-HU_{triMe} inhibiting HCT116 cell proliferation at a lower concentration, as shown in Figure S4. Statistical analyses of results for complex I- and complex III-induced oxygen consumption as a function of different Mito-HUs (Figure 2) are shown in Tables S3 and S4, respectively.

Next, we investigated in detail the relationship between the different Mito-HU analogs (Table 1) and the extent of inhibition effects of cell proliferation and mitochondrial complex activities. There is a strong linear fit ($R^2 = 0.9996$, Figure S8) between alkyl side chain length and relative hydrophobicity (log P, Table 1). First, we analyzed the correlation between the chain length and hydrophobicity of Mito-HUs and their antiproliferative effects (Figure 3). Figure 3A shows the relationship between the chain length (left) and hydrophobicity (right) as a function of a fold-increase in antiproliferative potency (compared with Mito₁₀-HU taken as unity). Results indicate an excellent degree of correlation (95% confidence band, $R^2 = 0.965$) between

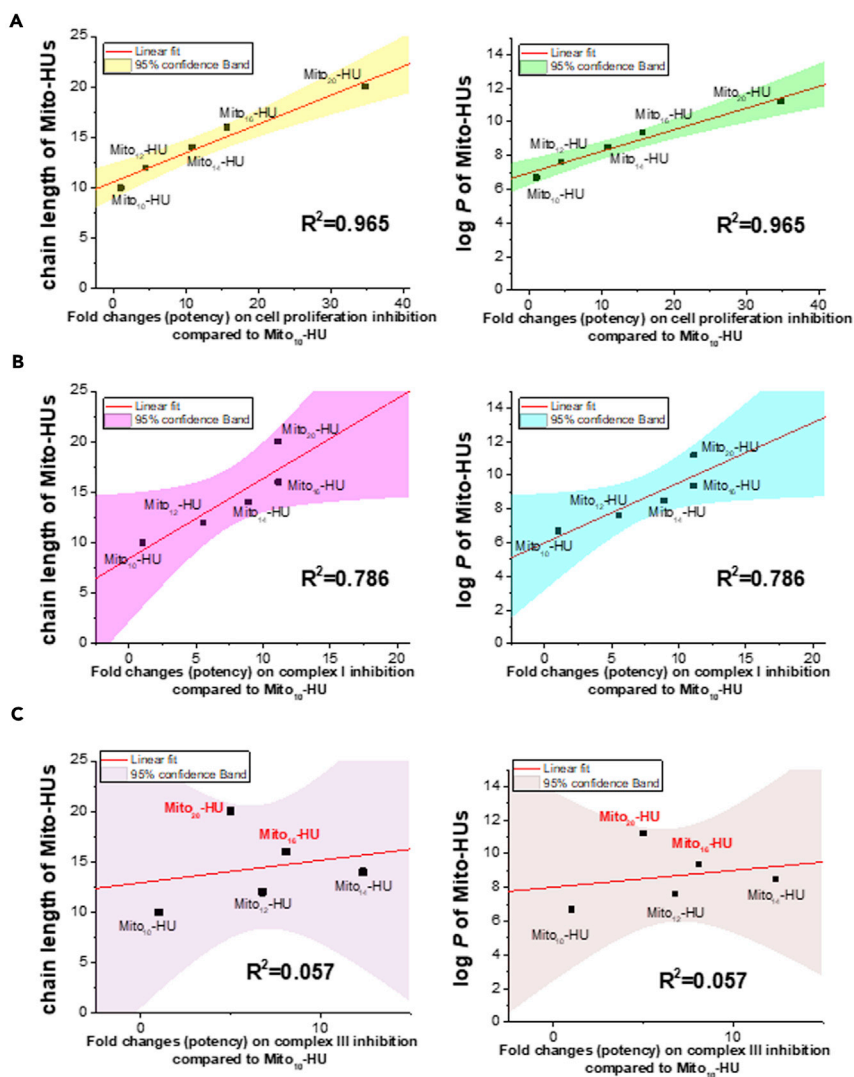


Figure 3. Relationship between Mito-HUs and inhibitions of cell proliferation or complex I/III activities in HCT116 cells

The chain lengths (*left*) and log Ps (*right*) of the Mito-HUs are plotted against the fold changes (potency) compared to the IC₅₀ values of Mito₁₀-HU for (A) cell proliferation, (B) mitochondrial complex I, and (C) complex III activities. The IC₅₀ values used to calculate the fold changes are from Figures 1 and 2, respectively. Data shown are the means ± SD.

increasing chain length/hydrophobicity and inhibition of proliferation in HCT116 cells treated with Mito-HUs, and that the antiproliferative effects of the Mito-HUs increase with the increasing hydrophobicity of the Mito-HUs. The correlation between the chain length/hydrophobicity and inhibition of mitochondrial complex I- and complex III-induced oxygen consumption revealed that the extent of inhibition of complex I- but not complex III-induced oxygen consumption is more linearly related to the increasing chain length and hydrophobicity of the Mito-HUs (Figures 3B and 3C). However, there is a good linear fit for the chain length of Mito-HUs up to 14 and inhibition of complex III-induced oxygen consumption (Figure S9). These results indicate that the inhibitory effects of Mito-HUs on complex III are maximal at chain length 14, and further increasing the chain length decreases the effectiveness on complex III inhibition.

Furthermore, we determined the functional changes in mitochondria induced by Mito-HU. Treatment with Mito-HU and another drug that targets the monocarboxylate transporter in mitochondria synergistically inhibited proliferation (Figure S10). A representative example is shown in Figure S10A, using a concentration at which Mito₁₀-HU and syrosingopine, an inhibitor of MCT-1/MCT-4-mediated lactate transport,

minimally affected cell proliferation. However, treatment with both Mito₁₀-HU and syrosingopine at these concentrations elicited a dramatic decrease in proliferation (Figure S10A). The combination index values show that the dual inhibition of cell proliferation induced by Mito₁₀-HU and syrosingopine is synergistic (Figure S10B). These results are consistent with the previous report on dual inhibition induced by metformin, a weak inhibitor of mitochondrial NADH dehydrogenase, and syrosingopine in cancer cells (Benjamin et al., 2018).

Immunomodulatory effects of Mito-HU with varying hydrophobicities

Published reports suggest that selective targeting and inhibition of mitochondrial complex III mitigate and reverse immunosuppression by T_{regs}, promoting the function of T_{eff} cells (Weinberg et al., 2019; Das et al., 2019). To investigate the effects of Mito₁₀-HU on T_{eff} versus T_{regs}, naive CD4⁺ T cells were isolated from SMARTA triple reporter mice and activated *in vitro* with GP₆₁₋₈₀ peptide (1 μg/mL) in the presence of TGFβ (5 ng/mL) and IL-2 (100 μg/mL) to induce T_{reg} differentiation, as described in the STAR Methods section. The CD4⁺ T cells were treated with Mito₁₀-HU at varying concentrations. As shown in Figure 4A, which depicts the gating strategies to assess these T cells, only live cells were gated out for further functional analysis. After six days, cells were stained to assess viability, phenotype, and function using flow cytometry. Results demonstrate that Mito₁₀-HU (Figures 4A–4C) inhibited FOXP3⁺ T_{reg} differentiation and/or survival and promoted T_{eff} IFNγ production. Next, we investigated the effect of different Mito-HUs with varying hydrophobicities (Mito₁₂-HU, Mito₁₄-HU, Mito₁₆-HU, and Mito₂₀-HU (Figure S11). Table S5 lists the concentrations of Mito-HUs presented in Figures 4B and S11 that have the maximum effect on IFNγ-YFP. As shown in Table S5, the most hydrophobic Mito-HU (e.g., Mito₂₀-HU) elicited the maximal effect on T_{eff} activation at the lowest concentration (0.3 μM).

Next, we investigated the effects of different Mito-HUs on immunosuppressive cells found in the TME. MDSCs have been shown to suppress CD8 T cells using several mechanisms including elevated generation of reactive oxygen species (Kawano et al., 2015). MDSCs consist of two distinct subsets of cells: M-MDSCs, which are characterized by the surface markers CD11b⁺, F4/80[−], Ly6C⁺, and Ly6G[−], and suppressive neutrophils or polymorphonuclear MDSCs (PMN-MDSCs), which express the surface markers CD11b⁺, F4/80⁺, Ly6C⁺, and Ly6G⁺ in mice (Veglia et al., 2018). Intriguingly, suppressive neutrophils differentiate from a Ly6C⁺, Ly6G[−], and cKit⁺ monocytic-like precursor of granulocytes primarily in the spleen (Mastio et al., 2019). A similar gating strategy employed for T cells was used in all MDSC differentiation assays, which were tested only on live cells after treatments. The results indicate the effects of Mito-HUs on the distributions/percentage populations of live cells at different stages of MDSC differentiation. The schematic representation of MDSC differentiation is shown in Figure 5A. Mito₁₄-HU reduced the frequency of M-MDSCs (Figure 5B). Figures 5B and 5C show that Mito₁₄-HU dose-dependently inhibited M-MDSC and suppressive neutrophils. Next, we investigated the effect of different Mito-HUs with varying hydrophobicities. Figure 5D shows the dose-dependent effects of Mito₁₀-HU, Mito₁₂-HU, Mito₁₄-HU, Mito₁₆-HU, and Mito₂₀-HU on the frequency of M-MDSCs. The IC₅₀ values for the different Mito-HUs are 9.6 μM, 2.6 μM, 0.89 μM, 0.44 μM, and 0.44 μM, respectively (Figure 5D). Figure 5E shows the effect of Mito-HUs on suppressive neutrophils. More hydrophobic Mito-HUs (Mito₁₄-HU, Mito₁₆-HU) demonstrated greater inhibitory effects on suppressive neutrophils (Figure 5E). These results suggest that more hydrophobic Mito-HUs inhibit both M-MDSCs and suppressive neutrophils.

DISCUSSION

In this study, we show that TPP⁺-conjugated Mito-HUs with varying alkyl side chain lengths potently increase their antiproliferative effects in colon cancer and other cancer cells. We also report that fine-tuning the hydrophobicity of mitochondria-targeted TPP⁺-conjugated compounds (Asin-Cayuela et al., 2004) could enhance their antiproliferative efficacy in tumor cells and modulate immune function. Results show that increasing the alkyl side chain to a 20-carbon analog (Mito₂₀-HU) inhibits the proliferation of HCT116 human colon cancer cells (IC₅₀ = 0.23 μM; log P = 11.2) much more effectively than Mito₁₀-HU (IC₅₀ = 8.0 μM; log P = 6.7). As shown in Table 2, substitution of the TPP⁺ group with methyl (-CH₃), trifluoromethyl (-CF₃), and chlorine (-Cl) substituents increases the hydrophobicity of Mito₁₀-HU. In future studies, it will be of interest to investigate the hydrophobic effect of the substituted TPP⁺ group on the mitochondrial targeting of complex I and complex III.

Reports indicate that mitochondria play an important role in modulating immune function (Weinberg et al., 2019). In the TME, cytotoxic T cells and antitumor M1 macrophages typically depend on glycolysis.

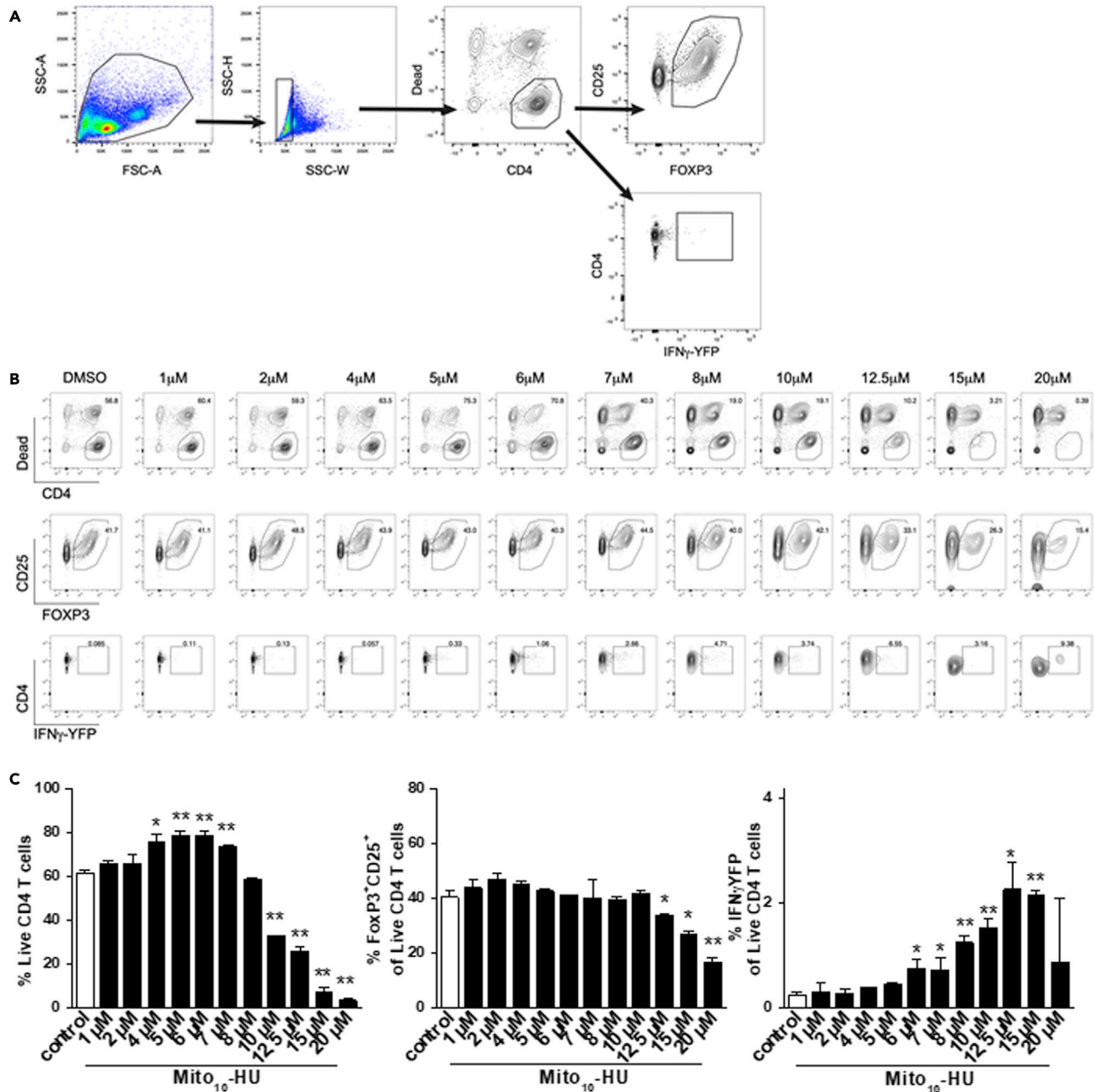


Figure 4. Effects of Mito₁₀-HU on *in vitro* differentiation of CD4 T cells

(A) The gating strategy reflects data from one DMSO control sample. First, the total population of cells was gated (FSC-A vs SSC-A). Then, single cells were gated (SSC-W vs SSC-H). Within the single cell population, we gated on the live CD4 T cells using a fixable LIVE/DEAD stain (CD4 vs DEAD). Within the live CD4 T cells we gated on CD25⁺FOXP3⁺ T_{regs} (FOXP3 vs CD25), as well as IFN γ -YFP⁺ CD4 T cells (IFN γ -YFP vs CD4).

(B) Live CD4 T cells were gated within the single cell populations, at varying concentrations of Mito₁₀-HU, along with DMSO controls (B, top row).

CD25⁺FOXP3⁺ T_{regs} (B, middle row) and IFN γ -YFP⁺ CD4 T cells (B, bottom row) were gated within the live CD4 T cell populations, at varying concentrations of Mito₁₀-HU, along with DMSO controls.

(C) Effects of Mito₁₀-HU on live CD4⁺ T cells within the lymphocyte gate (C, left), the frequency of FOXP3⁺CD25⁺ cells within the live CD4⁺ T cells (C, middle), and T_{eff} function is shown as the frequency of IFN γ -YFP positive cells within the live CD4⁺ T cells (C, right). Data shown are the means \pm SD, n = 2 per treatment group. *p < 0.05, **p < 0.01 vs control.

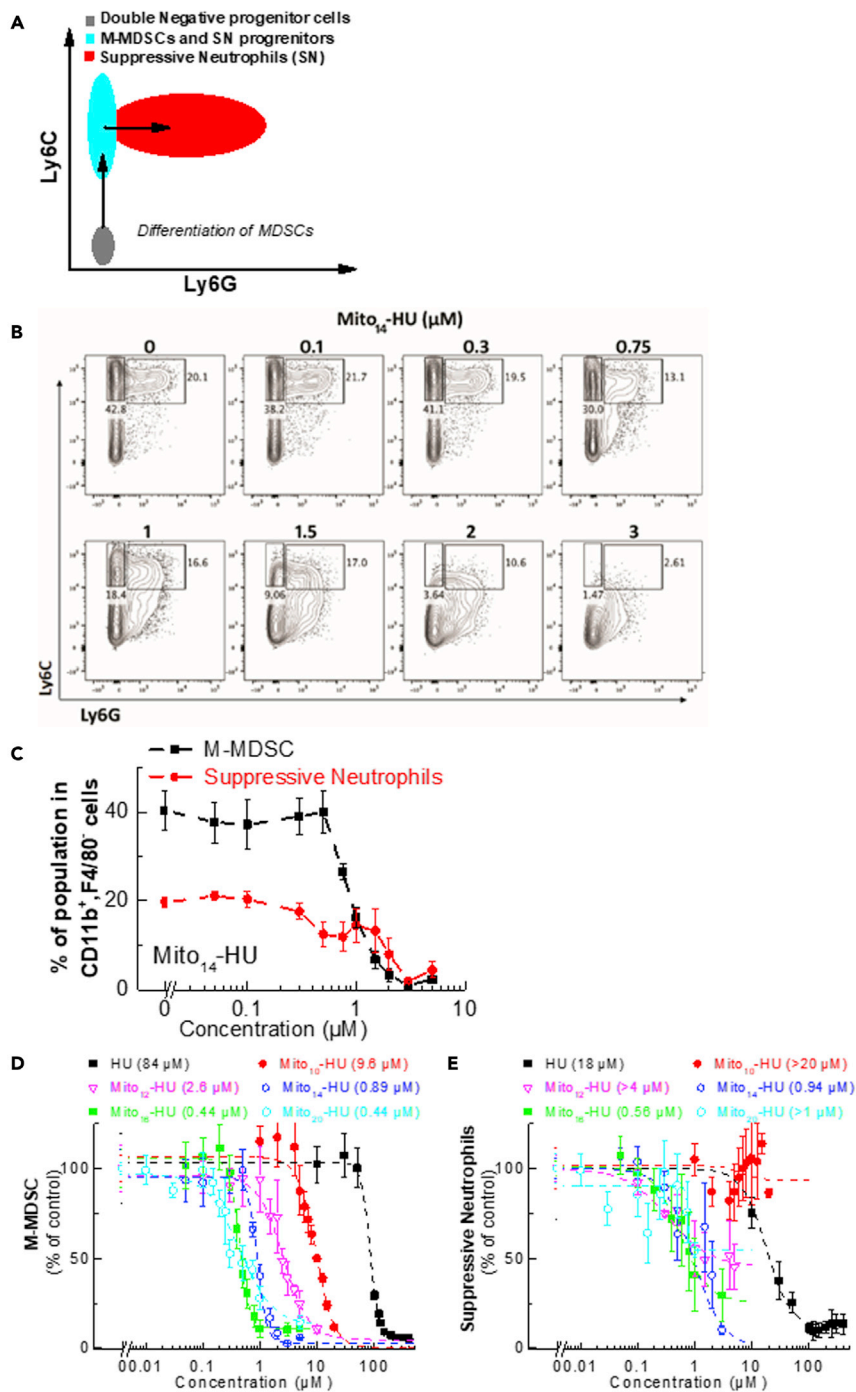


Figure 5. In vitro differentiation of MDSCs and suppressive neutrophils in the presence of different concentrations of Mito₁₄-HU and Mito-HUs with varying hydrophobicities

(A) Scheme of differentiation of MDSCs.

(B) Representative flow cytometry contour plots of *in vitro* differentiation of MDSCs under varying concentrations of Mito₁₄-HU using FlowJo Software (FlowJo Software, 2019).

(C) Summary data depicting distribution of MDSCs after three days treatment with Mito₁₄-HU generated from panel (B).

(D and E) (D) Dose-dependent effects of Mito-HUs with different side chain lengths on M-MDSC and (E) suppressive neutrophils. Dashed lines represent the fitting curves used for determination of the IC₅₀ values. Data shown are the means ± SD.

Table 2. Calculated partition coefficients and relative hydrophobic regions in Mito-HUs with substituted TPP

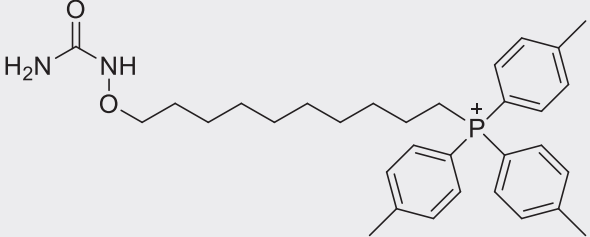
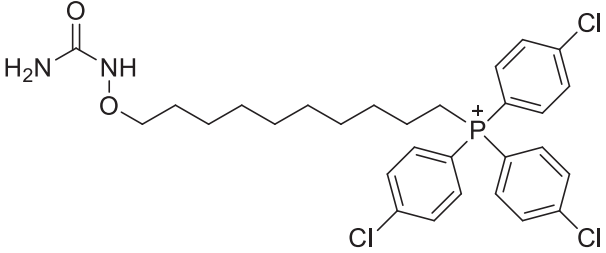
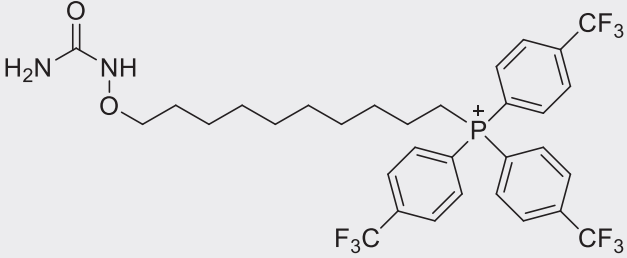
Molecule	Structure	log P*
Mito ₁₀ -HU _{triMe}		8.3
Mito ₁₀ -HU _{triCl}		8.5
Mito ₁₀ -HU _{triCF3}		9.4

Figure 2 shows three 3D surface representations of the Mito-HU protein structure, colored by relative hydrophobicity. The top structure (Mito₁₀-HU_{triMe}) shows a protein with a red and blue surface. The middle structure (Mito₁₀-HU_{triCl}) shows a protein with a blue and red surface. The bottom structure (Mito₁₀-HU_{triCF3}) shows a protein with a blue and red surface.

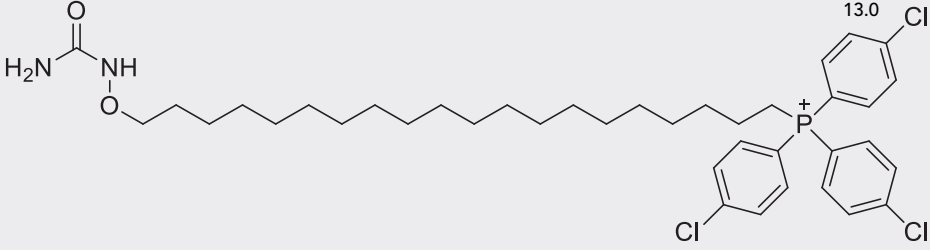
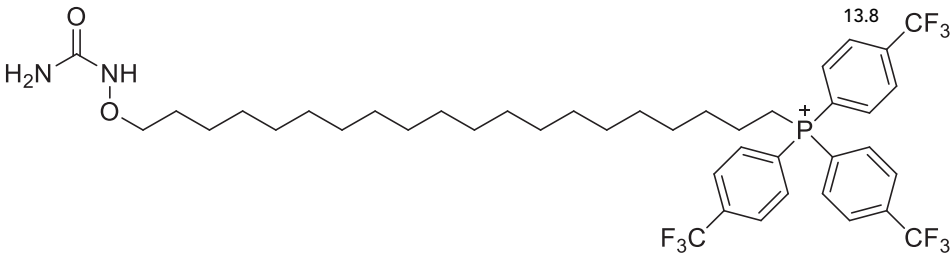
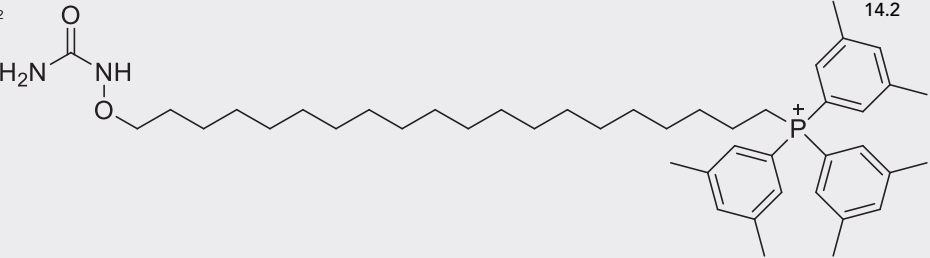
(Continued on next page)

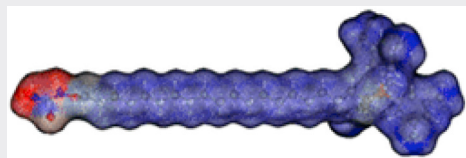
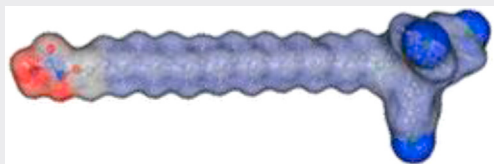
Table 2. Continued

Molecule	Structure	log P*
Mito ₁₀ -HU _{triMe2}		9.8
Mito ₂₀ -HU _{triMe}		12.7
Mito ₂₀ -HU _{triOMe}		10.7

(Continued on next page)

Table 2. Continued

Molecule	Structure	log P*
Mito ₂₀ -HU _{triCl}		13.0
Mito ₁₀ -HU _{triCF3}		13.8
Mito ₁₀ -HU _{triMe2}		14.2



However, other cells in the TME—such as the immunosuppressive M2 macrophages, MDSCs, or T_{regs} —depend on mitochondrial functions including OXPHOS (Weinberg et al., 2019). Molecular profiling studies in melanoma patients revealed considerable immunosuppression and increased expression of OXPHOS genes in melanoma brain metastases compared with extracranial metastases (Fischer et al., 2019). Under these conditions, the OXPHOS inhibitor IACS-010759 effectively blocked the formation of metastases. In the present study, we show that Mito-HUs inhibited MDSCs and that increasing the hydrophobicity of Mito-HU dose-dependently enhanced the inhibition of MDSCs (Figure 5). The IC_{50} value for Mito₂₀-HU to inhibit M-MDSCs is 0.44 μM as compared with 9.6 μM for Mito₁₀-HU (Figure 5). These findings show that TPP^+ containing mitochondria-targeted compounds exhibits similar dose-response effects in cancer cells and in immunosuppressive cells in the TME.

The TME provides a proinflammatory environment that facilitates tumor growth. High levels of reactive oxygen and nitrogen species generated potentially by MDSCs in the TME are cytotoxic to T cells and, thus, cripple their ability to destroy tumor cells (Corzo et al., 2009; Groth et al., 2019). T_{regs} suppress antitumor immunity that essentially hampers immunotherapy. Drugs inhibiting mitochondrial complex III have been shown to reverse the immunosuppressive function of T_{regs} (Weinberg et al., 2019). Because hydrophobic Mito-HUs can inhibit both complex I- and complex III-induced mitochondrial oxygen consumption, we tested whether Mito-HU can inhibit the T_{regs} population while increasing the population of T_{effs} . As shown in Figure 4, Mito₁₀-HU inhibited T_{reg} differentiation and/or survival while stimulating T_{effs} . Reactive oxygen and nitrogen species generated by MDSCs have been shown to suppress the function and proliferation of T cells (Feng et al., 2018). Both NADPH oxidase 2, a source of superoxide, and inducible nitric oxide synthase, a source of nitric oxide, have been implicated in T cell suppression. Previous studies showed that administration of mitochondria-targeted drugs (e.g., Mito-apocynin) in MitoPARK mice inhibited the expression of NADPH oxidase 2 and inducible nitric oxide synthase, as well as the oxidative and nitritative damage in mitochondrial proteins and inflammation in glial cells (Langley et al., 2017). Mitochondria-targeted honokiol suppressed the phosphorylation of mitoSTAT3 (Pan et al., 2018). STAT3 (signal transducer and activator of transcription 3) is involved in the immunosuppression observed in pancreatic cancer patients (Trovato et al., 2019). Future studies will focus on testing these mechanisms for Mito-HUs. It is likely that modulating the hydrophobicity of Mito-HUs may play a key role in activating the antitumor immune response.

Depending on the alkyl side chain length, the calculated hydrophobicity, or the lipid-to-water partition coefficients ($\log P$), of Mito-HU varies (Table 1). Because HU is very water-soluble ($\log P = -1.8$), Mito₄-HU containing a four-carbon alkyl side chain is still hydrophilic ($\log P = 4.0$) and a substantial increase in hydrophobicity was noticeable only in Mito-HUs with a much longer alkyl chain with $n \geq 10$ (e.g., Mito₁₀-HU, Mito₁₆-HU, Mito₂₀-HU) (Table 1). Results show that with increasing hydrophobicity, the antiproliferative potency of Mito-HUs dramatically increased (Figure 1 and Table S2). In contrast to HU, which had a negligible effect on mitochondrial oxygen consumption, Mito-HUs (Mito₁₀-HU, Mito₁₂-HU, Mito₁₆-HU, and Mito₂₀-HU) inhibited both mitochondrial complex I- and complex III-induced oxygen consumption at low micromolar concentrations (Figure 2 and Tables S3 and S4).

Mito₄-HU, with a TPP^+ moiety containing a four-carbon side chain, is anomalous in that its antiproliferative efficacy is lower than that of HU. In contrast, attaching a four-carbon alkyl side chain to a hydrophobic molecule has previously been shown to substantially increase its hydrophobicity and antiproliferative efficacy (Cheng et al., 2020a). HU exerts its cytostatic mechanism of action primarily through inhibition of RDR in proliferating cells. HU inhibits the tyrosyl radical that is required for RDR activity (Lassmann et al., 1992). The tyrosyl radical in RDR also participates in a long-range electron transfer to a cysteinyl residue located on the surface of RDR, forming a cysteinyl thiyl radical (Zhang et al., 2005; Chang et al., 2004), and it is likely that HU reacts with the radical on the surface and inhibits the activity.

The free radical mechanism is not viable once the OH group is derivatized. Thus, the antiproliferative mechanism of action of Mito-HUs differs from that of HU. Because HU is intrinsically very hydrophilic, it is necessary to conjugate HU with TPP^+ containing much longer alkyl side chain lengths to increase the hydrophobicity of Mito-HUs as shown: Mito₁₀-HU ($\log P = 6.7$), Mito₁₂-HU ($\log P = 7.6$), Mito₁₆-HU ($\log P = 9.4$), and Mito₂₀-HU ($\log P = 11.2$).

Previous reports suggest that replacing the OH group in HU with an alkyl group inhibits its antiproliferative effect due to the lack of a tyrosyl or cysteinyl radical scavenging mechanism (Singh and Xu, 2016). However, replacing the OH group with alkyl-substituted TPP^+ potently stimulates the antiproliferative mechanism

that is dependent on the alkyl side chain length. Results show that Mito₄-HU (log P = 4.0) did not inhibit the proliferation of MiaPaCa-2 cells, whereas Mito₁₀-HU (log P = 6.7), Mito₁₂-HU (log P = 7.6), Mito₁₆-HU (log P = 9.4), and Mito₂₀-HU (log P = 11.2) with increasing hydrophobicity exhibited increasing antiproliferative potencies. This suggests that replacement of the -OH group with the hydrophobic cationic substituent alters their mechanism of action in cancer cells.

The radiation sensitizing property of HU is well established (Leyden et al., 2000). HU arrests cells in the S-phase by inhibiting the R2 subunit of the ribonucleotide reductase and DNA synthesis (Zhou et al., 2013; Yarbro, 1992). The activity of topoisomerases is maximal during DNA replication. Radiation inhibits DNA replication, inhibits DNA repair, and is more effective in tumor cells treated with a cytostatic agent.

Mitochondria-targeted drugs are also effective hypoxic radiation sensitizers (Chang et al., 2004). This effect, however, arises from inhibiting mitochondrial respiration. Radiation is not very effective under hypoxic conditions in eradicating tumor cells. Inhibiting mitochondrial respiration can effectively increase the oxygen concentration in hypoxic regions of tumor cells. As a result, inhibition of mitochondrial respiration has been shown to augment the efficacy of radiation therapy (Cheng et al., 2016; Ashton et al., 2018). Thus, combining Mito-HUs with radiation may be more effective in killing hypoxic tumor cells.

The immunomodulatory effects of Mito-HU are dependent on the alkyl side chain length. More hydrophobic Mito-HUs inhibited M-MDSCs and suppressive neutrophils at submicromolar concentrations (Figure 5). The potency of inhibition increased with increasing side chain lengths. Mito-HUs inhibited proliferation of the colon cancer cells and M-MDSCs with a similar dose dependency. This class of mitochondria-targeted and structurally modified FDA-approved antitumor drugs could also play an important role in inhibiting metastatic tumors exhibiting enhanced immunosuppression and OXPHOS.

Limitations of the study

We acknowledge the limitations of the present study. Although the *in vitro* model clearly shows that with increasing hydrophobicity, Mito-HUs strongly inhibit the survival of M-MDSCs or the differentiation of the double-negative progenitor cells to M-MDSC (Figure 5), a similar trend is less clear in suppressive neutrophils, especially with more hydrophobic Mito-HUs (e.g., Mito₁₈-HU, Mito₂₀-HU). This may be due to the decreased levels of monocytic-like precursor of granulocytes that further differentiate into neutrophils. We have not yet investigated the tumor regressing effects of Mito-HUs in an *in vivo* mouse model. However, we have previously shown that mitochondria-targeted drugs cause regression of tumors in mice xenografts (Cheng et al., 2013, 2016, 2020b; Boyle et al., 2018). To fully understand the antitumor immune mechanism of Mito-HU in an *in vivo* setting, it is essential to perform studies in immune-competent mice.

STAR★METHODS

Detailed methods are provided in the online version of this paper and include the following:

- KEY RESOURCES TABLE
- RESOURCE AVAILABILITY
 - Lead contact
 - Materials availability
 - Data and code availability
- EXPERIMENTAL MODEL AND SUBJECT DETAILS
 - Cell lines
 - Animals
- METHOD DETAILS
 - Syntheses of Mito-HUs
 - Cell proliferation measurements
 - Cytotoxicity assay
 - Mitochondrial oxygen consumption measurements
 - Immunoregulatory measurements
- QUANTIFICATION AND STATISTICAL ANALYSIS

SUPPLEMENTAL INFORMATION

Supplemental information can be found online at <https://doi.org/10.1016/j.isci.2021.102673>.

ACKNOWLEDGMENTS

This work was supported in part by The Harry R. & Angeline E. Quadracci Professor in Parkinson's Research Endowment (B.K.).

AUTHOR CONTRIBUTIONS

G.C., P.T., and P.V. performed the *in vitro* experiments and analysis. M.H. and B.K. designed and supervised the synthesis of the compounds and provided chemistry support. B.K. and W.C. designed and supervised the studies. G.C. analyzed the Seahorse and IncuCyte data. P.T., R.Z., and G.C. analyzed T_{reg} data. P.V. and G.C. analyzed MDSC data. G.C. and B.K. initiated the study. G.C., M.H., P.T., P.V., W.C., and B.K. prepared and reviewed the manuscript.

DECLARATION OF INTERESTS

G.C., M.H., and B.K. are the inventors of a US provisional patent application (63/141,802) filed on January 26, 2021.

Received: January 27, 2021

Revised: April 8, 2021

Accepted: May 27, 2021

Published: June 25, 2021

REFERENCES

- American Association for Cancer Research (2019). Drugging OXPHOS dependency in cancer. *Cancer Discov.* 9, O10.
- Ashton, T.M., Mckenna, W.G., Kunz-Schughart, L.A., and Higgins, G.S. (2018). Oxidative phosphorylation as an emerging target in cancer therapy. *Clin. Cancer Res.* 24, 2482–2490.
- Asin-Cayuela, J., Manas, A.-R.B., James, A.M., Smith, R.A.J., and Murphy, M.P. (2004). Fine-tuning the hydrophobicity of a mitochondria-targeted antioxidant. *FEBS Lett.* 571, 9–16.
- Benjamin, D., Robay, D., Hindupur, S.K., Pohlmann, J., Colombi, M., El-Shemerly, M.Y., Maira, S.M., Moroni, C., Lane, H.A., and Hall, M.N. (2018). Dual inhibition of the lactate transporters MCT1 and MCT4 is synthetic lethal with metformin due to NAD⁺ depletion in cancer cells. *Cell Rep.* 25, 3047–3058.e4.
- Boyle, K.A., Van Wickle, J., Hill, R.B., Marchese, A., Kalyanaraman, B., and Dwinell, M.B. (2018). Mitochondria-targeted drugs stimulate mitophagy and abrogate colon cancer cell proliferation. *J. Biol. Chem.* 293, 14891–14904.
- Chanda, S., and Ramakrishnan, S. (2015). Poly(alkylene itaconate)s – an interesting class of polyesters with periodically located exo-chain double bonds susceptible to Michael addition. *Polym. Chem.* 6, 2108–2114.
- Chang, M.C.Y., Yee, C.S., Stubbe, J., and Nocera, D.G. (2004). Turning on ribonucleotide reductase by light-initiated amino acid radical generation. *Proc. Natl. Acad. Sci. U S A* 101, 6882.
- Cheng, G., Hardy, M., Topchyan, P., Zander, R., Volberding, P., Cui, W., and Kalyanaraman, B. (2020a). Potent inhibition of tumour cell proliferation and immunoregulatory function by mitochondria-targeted atovaquone. *Sci. Rep.* 10, 17872.
- Cheng, G., Hardy, M., Zielonka, J., Weh, K.M., Zielonka, M., Boyle, K., Abu Eid, M., Mcallister, D., Bennett, B., Kresty, L.A., et al. (2020b). Mitochondria-targeted magnolol inhibits OXPHOS, proliferation, and tumor growth via modulation of energetics and autophagy in melanoma cells. *Cancer Res. Treat. Commun.* 25, 100210.
- Cheng, G., Zhang, Q., Pan, J., Lee, Y., Ouari, O., Hardy, M., Zielonka, M., Myers, C.R., Zielonka, J., Weh, K., et al. (2019). Targeting lonidamine to mitochondria mitigates lung tumorigenesis and brain metastasis. *Nat. Commun.* 10, 2205.
- Cheng, G., Zielonka, J., Dranka, B.P., Mcallister, D., Mackinnon, A.C., Jr., Joseph, J., and Kalyanaraman, B. (2012). Mitochondria-targeted drugs synergize with 2-deoxyglucose to trigger breast cancer cell death. *Cancer Res.* 72, 2634–2644.
- Cheng, G., Zielonka, J., Mcallister, D.M., Mackinnon, A.C., Jr., Joseph, J., Dwinell, M.B., and Kalyanaraman, B. (2013). Mitochondria-targeted vitamin E analogs inhibit breast cancer cell energy metabolism and promote cell death. *BMC Cancer* 13, 285.
- Cheng, G., Zielonka, J., Ouari, O., Lopez, M., Mcallister, D., Boyle, K., Barrios, C.S., Weber, J.J., Johnson, B.D., Hardy, M., et al. (2016). Mitochondria-targeted analogues of metformin exhibit enhanced antiproliferative and radiosensitizing effects in pancreatic cancer cells. *Cancer Res.* 76, 3904–3915.
- Corzo, C.A., Cotter, M.J., Cheng, P., Cheng, F., Kusmartsev, S., Sotomayor, E., Padhya, T., Mccaffrey, T.V., Mccaffrey, J.C., and Gabrilovich, D.I. (2009). Mechanism regulating reactive oxygen species in tumor-induced myeloid-derived suppressor cells. *J. Immunol.* 182, 5693–5701.
- Das, M., Alzaid, F., and Bayry, J. (2019). Regulatory T cells under the mercy of mitochondria. *Cell Metab.* 29, 243–245.
- Feng, S., Cheng, X., Zhang, L., Lu, X., Chaudhary, S., Teng, R., Frederickson, C., Champion, M.M., Zhao, R., Cheng, L., et al. (2018). Myeloid-derived suppressor cells inhibit T cell activation through nitrating LCK in mouse cancers. *Proc. Natl. Acad. Sci. U S A* 115, 10094–10099.
- Fiorillo, M., Lamb, R., Tanowitz, H.B., Mutti, L., Krstic-Demonacos, M., Cappello, A.R., Martinez-Outschoorn, U.E., Sotgia, F., and Lisanti, M.P. (2016). Repurposing atovaquone: targeting mitochondrial complex III and OXPHOS to eradicate cancer stem cells. *Oncotarget* 7, 34084–34099.
- Fischer, G.M., Jalali, A., Kircher, D.A., Lee, W.C., Mcquade, J.L., Haydu, L.E., Joon, A.Y., Reuben, A., De Macedo, M.P., Carapeto, F.C.L., et al. (2019). Molecular profiling reveals unique immune and metabolic features of melanoma brain metastases. *Cancer Discov.* 9, 628–645.
- FlowJo Software (2019). FlowJo Software, Tenth Edition (Becton, Dickinson and Company).
- Groth, C., Hu, X., Weber, R., Fleming, V., Altevogt, P., Utikal, J., and Umansky, V. (2019). Immunosuppression mediated by myeloid-derived suppressor cells (MDSCs) during tumour progression. *Br. J. Cancer* 120, 16–25.
- Grund, F.M., Armitage, J.O., and Burns, C.P. (1977). Hydroxyurea in the prevention of the effects of leukostasis in acute leukemia. *Arch. Intern. Med.* 137, 1246–1247.
- Hossain, F., Al-Khami, A.A., Wyczechowska, D., Hernandez, C., Zheng, L., Reiss, K., Valle, L.D., Trillo-Tinoco, J., Maj, T., Zou, W., et al. (2015). Inhibition of fatty acid oxidation modulates immunosuppressive functions of myeloid-derived suppressor cells and enhances cancer therapies. *Cancer Immunol. Res.* 3, 1236–1247.

- Kawano, Y., Moschetta, M., Manier, S., Glavey, S., Görgün, G.T., Roccaro, A.M., Anderson, K.C., and Ghobrial, I.M. (2015). Targeting the bone marrow microenvironment in multiple myeloma. *Immunol. Rev.* 263, 160–172.
- Klopman, G., Li, J.-Y., Wang, S., and Dimayuga, M. (1994). Computer automated log P calculations based on an extended group contribution approach. *J. Chem. Inf. Comput. Sci.* 34, 752–781.
- Koç, A., Wheeler, L.J., Mathews, C.K., and Merrill, G.F. (2004). Hydroxyurea arrests DNA replication by a mechanism that preserves basal dNTP pools. *J. Biol. Chem.* 279, 223–230.
- Langley, M., Ghosh, A., Charli, A., Sarkar, S., Ay, M., Luo, J., Zielonka, J., Brenza, T., Bennett, B., Jin, H., et al. (2017). Mito-apocynin prevents mitochondrial dysfunction, microglial activation, oxidative damage, and progressive neurodegeneration in MitoPark transgenic mice. *Antioxid. Redox Signal.* 27, 1048–1066.
- Lassmann, G., Thelander, L., and Gräslund, A. (1992). EPR stopped-flow studies of the reaction of the tyrosyl radical of protein R2 from ribonucleotide reductase with hydroxyurea. *Biochem. Biophys. Res. Commun.* 188, 879–887.
- Law, A.M.K., Valdes-Mora, F., and Gallego-Ortega, D. (2020). Myeloid-derived suppressor cells as a therapeutic target for cancer. *Cells* 9, 561.
- Leyden, D., Ahmed, N., and Hassan, H.T. (2000). Hydroxyurea and trimidox enhance the radiation effect in human pancreatic adenocarcinoma cells. *Anticancer Res.* 20, 133–138.
- Madaan, K., Kaushik, D., and Verma, T. (2012). Hydroxyurea: a key player in cancer chemotherapy. *Expert Rev. Anticancer Ther.* 12, 19–29.
- Mai, X., Lu, X., Xia, H., Cao, Y., Liao, Y., and Lv, X. (2010). Synthesis, antitumor evaluation and crystal structure of hydroxyurea derivatives. *Chem. Pharm. Bull.* 58, 94–97.
- Mastio, J., Condamine, T., Dominguez, G., Kossenkov, A.V., Donthireddy, L., Veglia, F., Lin, C., Wang, F., Fu, S., Zhou, J., et al. (2019). Identification of monocyte-like precursors of granulocytes in cancer as a mechanism for accumulation of PMN-MDSCs. *J. Exp. Med.* 216, 2150–2169.
- Nagaraj, S., Youn, J.I., and Gabrilovich, D.I. (2013). Reciprocal relationship between myeloid-derived suppressor cells and T cells. *J. Immunol.* 191, 17–23.
- Oo, Z.Y., Proctor, M., Stevenson, A.J., Nazareth, D., Fernando, M., Daignault, S.M., Lanagan, C., Walpole, S., Bonazzi, V., Škalamera, D., et al. (2019). Combined use of subclinical hydroxyurea and CHK1 inhibitor effectively controls melanoma and lung cancer progression, with reduced normal tissue toxicity compared to gemcitabine. *Mol. Oncol.* 13, 1503–1518.
- Oxenius, A., Bachmann, M.F., Zinkernagel, R.M., and Hengartner, H. (1998). Virus-specific MHC-class II-restricted TCR-transgenic mice: effects on humoral and cellular immune responses after viral infection. *Eur. J. Immunol.* 28, 390–400.
- Pan, J., Lee, Y., Cheng, G., Zielonka, J., Zhang, Q., Bajzikova, M., Xiong, D., Tsaih, S.-W., Hardy, M., Flister, M., et al. (2018). Mitochondria-targeted honokiol confers a striking inhibitory effect on lung cancer via inhibiting complex I activity. *iScience* 3, 192–207.
- Reinhardt, R.L., Liang, H.-E., and Locksley, R.M. (2009). Cytokine-secreting follicular T cells shape the antibody repertoire. *Nat. Immunol.* 10, 385–393.
- Ren, S., Wang, R., Komatsu, K., Bonaz-Krause, P., Zyrianov, Y., McKenna, C.E., Csiipke, C., Tokes, Z.A., and Lien, E.J. (2002). Synthesis, biological evaluation, and quantitative Structure–Activity relationship analysis of new Schiff bases of hydroxysemicarbazide as potential antitumor agents. *J. Med. Chem.* 45, 410–419.
- Salabei, J.K., Gibb, A.A., and Hill, B.G. (2014). Comprehensive measurement of respiratory activity in permeabilized cells using extracellular flux analysis. *Nat. Protoc.* 9, 421–438.
- Saleh, R., and Elkord, E. (2020). FoxP3(+) T regulatory cells in cancer: prognostic biomarkers and therapeutic targets. *Cancer Lett.* 490, 174–185.
- Sawant, A., Schafer, C.C., Jin, T.H., Zmijewski, J., Tse, H.M., Roth, J., Sun, Z., Siegal, G.P., Thannickal, V.J., Grant, S.C., et al. (2013). Enhancement of antitumor immunity in lung cancer by targeting myeloid-derived suppressor cell pathways. *Cancer Res.* 73, 6609–6620.
- Shulman, Z., Gitlin, A.D., Weinstein, J.S., Lainez, B., Esplugues, E., Flavell, R.A., Craft, J.E., and Nussenzweig, M.C. (2014). Dynamic signaling by T follicular helper cells during germinal center B cell selection. *Science* 345, 1058–1062.
- Singh, A., and Xu, Y.J. (2016). The cell killing mechanisms of hydroxyurea. *Genes (Basel)* 7, 99.
- Solito, S., Falisi, E., Diaz-Montero, C.M., Doni, A., Pinton, L., Rosato, A., Francescato, S., Basso, G., Zanovello, P., Onicescu, G., et al. (2011). A human promyelocytic-like population is responsible for the immune suppression mediated by myeloid-derived suppressor cells. *Blood* 118, 2254–2265.
- Spivak, J.L., and Hasselbalch, H. (2011). Hydroxycarbamide: a user's guide for chronic myeloproliferative disorders. *Expert Rev. Anticancer Ther.* 11, 403–414.
- Teng, J., Hejazi, S., Hiddingh, L., Carvalho, L., De Gooijer, M.C., Wakimoto, H., Barazas, M., Tannous, M., Chi, A.S., Noske, D.P., et al. (2018). Recycling drug screen repurposes hydroxyurea as a sensitizer of glioblastomas to temozolomide targeting de novo DNA synthesis, irrespective of molecular subtype. *Neuro Oncol.* 20, 642–654.
- Trovato, R., Fiore, A., Sartori, S., Canè, S., Giugno, R., Cascione, L., Paiella, S., Salvia, R., De Sanctis, F., Poffe, O., et al. (2019). Immunosuppression by monocytic myeloid-derived suppressor cells in patients with pancreatic ductal carcinoma is orchestrated by STAT3. *J. Immunother. Cancer* 7, 255.
- Veglia, F., Perego, M., and Gabrilovich, D. (2018). Myeloid-derived suppressor cells coming of age. *Nat. Immunol.* 19, 108–119.
- Viswanadhan, V.N., Ghose, A.K., Revankar, G.R., and Robins, R.K. (1989). Atomic physicochemical parameters for three dimensional structure directed quantitative structure-activity relationships. 4. Additional parameters for hydrophobic and dispersive interactions and their application for an automated superposition of certain naturally occurring nucleoside antibiotics. *J. Chem. Inf. Comput. Sci.* 29, 163–172.
- Weinberg, S.E., and Chandel, N.S. (2015). Targeting mitochondria metabolism for cancer therapy. *Nat. Chem. Biol.* 11, 9–15.
- Weinberg, S.E., Singer, B.D., Steinert, E.M., Martinez, C.A., Mehta, M.M., Martinez-Reyes, I., Gao, P., Helmin, K.A., Abdala-Valencia, H., Sena, L.A., et al. (2019). Mitochondrial complex III is essential for suppressive function of regulatory T cells. *Nature* 565, 495–499.
- Weinstein, J.S., Herman, E.I., Lainez, B., Liconalimón, P., Esplugues, E., Flavell, R., and Craft, J. (2016). TFH cells progressively differentiate to regulate the germinal center response. *Nat. Immunol.* 17, 1197–1205.
- Wheaton, W.W., Weinberg, S.E., Hamanaka, R.B., Soberanes, S., Sullivan, L.B., Anso, E., Glasauer, A., Dufour, E., Mutlu, G.M., Budigner, G.S., and Chandel, N.S. (2014). Metformin inhibits mitochondrial complex I of cancer cells to reduce tumorigenesis. *Elife* 3, e02242.
- Xin, G., Schauder, D.M., Lainez, B., Weinstein, J.S., Dai, Z., Chen, Y., Esplugues, E., Wen, R., Wang, D., Parish, I.A., et al. (2015). A critical role of IL-21-induced BATF in sustaining CD8-T-cell-mediated chronic viral control. *Cell Rep.* 13, 1118–1124.
- Xin, G., Zander, R., Schauder, D.M., Chen, Y., Weinstein, J.S., Drobyski, W.R., Tarakanova, V., Craft, J., and Cui, W. (2018). Single-cell RNA sequencing unveils an IL-10-producing helper subset that sustains humoral immunity during persistent infection. *Nat. Commun.* 9, 5037.
- Xu, Y., Xue, D., Bankhead, A., 3rd, and Neamati, N. (2020). Why all the fuss about oxidative phosphorylation (OXPHOS)? *J. Med. Chem.* 63, 14276–14307.
- Yarbro, J.W. (1992). Mechanism of action of hydroxyurea. *Semin. Oncol.* 19, 1–10.
- Zhang, H., Xu, Y., Joseph, J., and Kalyanaraman, B. (2005). Intramolecular electron transfer between tyrosyl radical and cysteine residue inhibits tyrosine nitration and induces thyl radical formation in model peptides treated with myeloperoxidase, H₂O₂, and NO₂⁻: EPR SPIN trapping studies. *J. Biol. Chem.* 280, 40684–40698.
- Zhou, B., Su, L., Hu, S., Hu, W., Yip, M.L., Wu, J., Gaur, S., Smith, D.L., Yuan, Y.C., Synold, T.W., et al. (2013). A small-molecule blocking ribonucleotide reductase holoenzyme formation inhibits cancer cell growth and overcomes drug resistance. *Cancer Res.* 73, 6484–6493.

STAR★METHODS

KEY RESOURCES TABLE

REAGENT or RESOURCE	SOURCE	IDENTIFIER
Antibodies		
Ly6C	Biologend	Cat# 128015
Ly6G	Biologend	Cat# 127613
CD11b	Biologend	Cat# 101223
F4/80	Biologend	Cat# 123113
CD4	Biologend	Cat# 100460
CD25	Biologend	Cat# 102012
FOXP3	Invitrogen	Cat# 12-5773-82
LIVE/DEAD™ Fixable Violet Dead Cell Stain Kit	Invitrogen	Cat# L34964
S100A9	BD Biosciences	Cat# 566010
Chemicals, peptides, and recombinant proteins		
Hydroxyurea	Combi-Blocks	Cat# OR-0532
1,14-Tetradecanediol	Combi-Blocks	Cat# OR-0896
DMF	Fisher Scientific	Cat# AC348431000
CH ₂ Cl ₂	Fisher Scientific	Cat# 143SK4
Mito-HU derivatives	This manuscript	N/A
1,10-Dibromodecane	Alfa Aesar	Cat# A12357.22
Sodium sulfate	Sigma-Aldrich	Cat# 238597
Acetonitrile	Sigma-Aldrich	Cat# 34998
Acetic anhydride	Sigma-Aldrich	Cat# 8222781000
HBr	Sigma-Aldrich	Cat# 244260
Pentane	Sigma-Aldrich	Cat# 1071761000
Diethylether	Sigma-Aldrich	Cat# 673811
Bromodecane	Sigma-Aldrich	Cat# 145785
Triethylamine	Sigma-Aldrich	Cat# 90335
EtOH	Sigma-Aldrich	Cat# 1009861000
Carbonyldiimidazole (CDI)	Sigma-Aldrich	Cat# 115533
Potassium carbonate	Sigma-Aldrich	Cat# 209619
Pyruvate	Sigma-Aldrich	Cat# P2256
Malate	Sigma-Aldrich	Cat# M7397
Succinate	Sigma-Aldrich	Cat# S3674
(4-Bromobutyl)-triphenylphosphonium bromide	Sigma-Aldrich	Cat# 272132
Triphenylphosphine	Sigma-Aldrich	Cat# T84409
Tri(p-tolyl)phosphine	Sigma-Aldrich	Cat# 287830
Rotenone	Sigma-Aldrich	Cat# R8875
Malonate	Sigma-Aldrich	Cat# M1296
Antimycin A	Sigma-Aldrich	Cat# A8674
1,16-Hexadecanediol	TCI	Cat# H0552
Eicosanedioic acid	TCI	Cat# E0320

(Continued on next page)

Continued

REAGENT or RESOURCE	SOURCE	IDENTIFIER
Plasma Membrane Permeabilizer (PMP)	Agilent	Cat# 102504-100
Adenosine 5'-diphosphate monopotassium salt dihydrate (ADP)	Sigma-Aldrich	Cat# A5285
SYTOX Green	ThermoFisher	Cat# S7020
Digitonin	Sigma-Aldrich	Cat# D141
Syrosingopine	Sigma-Aldrich	Cat# SML1908

Experimental models: Cell lines

Human: MiaPaCa-2	American Type Culture Collection	Cat# CRL-1420
Human: HCT116	American Type Culture Collection	Cat# CCL-247

Experimental models: Organisms/strains

SMARTA triple reporter mice	This manuscript	N/A
GREAT (interferon-gamma reporter with endogenous polyA transcript) mice	Jackson Laboratory	Cat# 017581
10 BiT mice	Dr. Casey Weaver, University of Alabama at Birmingham	N/A
IL-21-tRFP mice	Dr. Joseph Craft, Yale University	N/A
SMARTA mice	Dr. Dorian McGavern, National Institutes of Health	N/A
C57bl/6 mice	Charles River	N/A

Other

RPMI 1640 Medium	Gibco	Cat# 11875093
Dulbecco's Modified Eagle Medium	Gibco	Cat# 11965118
Fetal bovine serum, qualified, USDA-approved regions	Omega Scientific, Inc.	Cat# FB-12

RESOURCE AVAILABILITY**Lead contact**

Further information and requests for resources and reagents should be directed to and will be fulfilled by the lead contact, Balaraman Kalyanaraman (balarama@mcw.edu).

Materials availability

The investigators have routinely made mitochondria-targeted agents available to other investigators upon request.

Data and code availability

This study did not generate/analyze any computational datasets/code.

EXPERIMENTAL MODEL AND SUBJECT DETAILS**Cell lines**

The following cell lines were obtained from the American Type Culture Collection (Manassas, VA), where they were regularly authenticated: HCT116 (ATCC Cat# CRL-247, human colon cancer cells) and MiaPaCa-2 (ATCC Cat# CRL-1420, human pancreatic cancer cells). All cells were cultured in a humidified incubator at 37°C and 5% carbon dioxide. HCT116 cells were maintained in RPMI 1640 medium (Thermo Fisher Scientific, Cat# 11875), supplemented with 10% fetal bovine serum. MiaPaCa-2 cells were maintained in Dulbecco's Modified Eagle Medium (Thermo Fisher Scientific, Waltham, MA; Cat# 11965) supplemented with 10% fetal bovine serum. All cells were stored in liquid nitrogen and used within 20 passages after thawing.

Animals

SMARTA triple reporter mice were generated in the following manner. First, IL-10 and IL-21 double-reporter mice (Xin et al., 2018) were generated by cross-breeding IL-21-tRFP mice (kindly provided by Dr. Joseph Craft, Yale University) (Xin et al., 2015; Weinstein et al., 2016; Shulman et al., 2014) with 10 BiT mice (kindly provided by Dr. Casey Weaver, University of Alabama at Birmingham). Double reporter mice were crossed with GREAT (interferon-gamma reporter with endogenous polyA transcript) mice (Reinhardt et al., 2009) from Jackson Laboratory (Bar Harbor, ME; Cat# 017581). These triple-reporter mice were then crossed with SMARTA mice (kindly provided by Dr. Dorian McGavern, National Institutes of Health) (Oxenius et al., 1998). Eight- to 12-week-old mice were used to generate T_{reg} cultures. Mice were bred and maintained in a closed breeding facility, and mouse handling conformed to the requirements of the Medical College of Wisconsin Institutional Animal Care and Use Committee guidelines. All experimental protocols were approved by the Medical College of Wisconsin Institutional Animal Care and Use Committee.

METHOD DETAILS

Syntheses of Mito-HUs

The Mito-HU derivatives were prepared by reacting HU with different halogeno-alkyltriphenylphosphonium salts in the presence of potassium carbonate at 70°C in N,N-dimethylformamide (DMF). In addition, the negative control, decyl-HU, was prepared by reacting bromodecane with HU using the same experimental conditions. To assess the relative hydrophobicities of HU and Mito-HUs, the octanol/water partition coefficients (log P) were calculated using a QSAR (quantitative structure-activity relationship) analysis and rational drug design (Table 1). This method also uses a consensus model built with ChemAxon software (San Diego, CA) (Viswanadhan et al., 1989; Klopman et al., 1994). Table 1 lists the log P values along with the calculated regions of the relative hydrophilic and hydrophobic regions. As shown in Table 1, there was a significant increase in the hydrophobicity of Mito-HU (as compared with HU) with the increasing alkyl side chain length (from C-4 to C-20).

General. All chemicals and organic solvents were commercially available and were used as supplied. The reactions were monitored by TLC using silica gel Merck $^{60}\text{F}254$. Crude materials were purified by flash chromatography on Merck Silica gel 60 (0.040–0.063 mm) or on a RediSep reverse phase C18 column. ^{31}P nuclear magnetic resonance (NMR), ^1H NMR and ^{13}C NMR spectra were recorded at 400.13 MHz spectrometers and 75.54 MHz, respectively. ^1H NMR spectra were recorded using a Bruker DPX AVANCE 400 spectrometer (Marseille, PACA, France) equipped with a quattro nucleus probe. Chemical shifts (δ) are reported in ppm and J values in Hertz.

A scheme of the synthesis of HUs is presented in the supplementary materials (Schemes S1–S3). NMR spectra and related parameters are given in Figures S12–S24.

Synthesis of 10-[(hydroxycarbamoyl)carbamoylamino]-decyltriphenylphosphonium trifluoroacetate (Mito₁₀-HU_{NHTPP+}). To a mixture of (10-aminodecyl)-triphenylphosphonium bromide (Cheng et al., 2016) (0.2 g, 0.37 mmol) and triethylamine (162 mL, 1.13 mmol) in dichloromethane (CH_2Cl_2), was added carbonyldiimidazole (CDI) (67 mg, 0.41 mmol) at 0°C. The mixture was stirred at room temperature for 4 hr. Then, HU (42 mg, 0.56 mmol) was added to the mixture with a few drops of DMF. The mixture was stirred at 50°C for 12 hr. Then, the precipitated product was dissolved in water (H_2O) and purified on chromatography reverse phase to deliver the corresponding Mito₁₀-HU_{NHTPP+} (51 mg, 23% yield).

High-resolution mass spectrometry (HRMS) calculated for Mito-HU_{NHTPP+} $\text{C}_{30}\text{H}_{39}\text{N}_3\text{O}_3\text{P}^+$ [M]⁺ 520.2724, found, 520.2723.

^{31}P NMR (400.13 MHz, $(\text{CD}_3)_2\text{SO}$) δ 24.05. ^1H NMR (400.13 MHz, $(\text{CD}_3)_2\text{SO}$) δ 7.96–7.73 (15H, m), 7.43 (1H, bs), 6.31 (1H, bs), 3.51–3.34 (2H, m), 3.15–3.95 (2H, m), 1.60–1.35 (6H, m), 1.33–1.14 (10H, m). ^{13}C NMR (75 MHz, $(\text{CD}_3)_2\text{SO}$) δ 159.8, 155.9, 134.87, 134.84, 133.6, 133.5, 130.3, 130.1, 118.9, 118.1, 40.6, 29.9, 29.8, 29.6, 29.1, 28.8, 28.7, 28.6, 28.0, 26.1, 21.7 (d, $J = 3.7$), 20.2 (d, $J = 49.9$).

Synthesis of 10-[(carbamoylamino)oxy]-decyl-tris-p-tolylphosphonium trifluoroacetate (Mito_{triMe}-HU). A mixture of 1,10-dibromodecane (5 g, 16.6 mmol) and tris-p-tolylphosphine (1 g, 3.2 mmol) was stirred at 80°C overnight. The reaction mixture was cooled. The residue was washed with diethyl ether (Et₂O). Purification by flash chromatography using pentane, Et₂O, and CH₂Cl₂/ethanol (EtOH; 9/1) as eluents successively delivered the corresponding (10-bromodecyl)-tris-p-tolylphosphonium (Mito_{triMe}-Br) (1.2 g, 60% yield).

HRMS calculated for Mito_{triMe}-Br C₃₁H₄₁BrP [M]⁺ 525.2108, found, 525.2113

³¹P (400.13 MHz, CDCl₃) δ 23.17. ¹H NMR (400.13 MHz, CDCl₃) δ 7.70-7.61 (6H, m), 7.50-7.44 (6H, m), 3.63-3.50 (2H, m), 3.38 (2H, t, J = 6.7 Hz), 2.47 (9H, s), 1.88-1.74 (3H, m), 1.64-1.52 (3H, m), 1.41-1.33 (2H, m), 1.28-1.17 (8H, m). ¹³C NMR (75 MHz, CDCl₃) δ 146.14, 146.11, 133.4, 133.3, 131.0, 131.0, 115.6, 114.7, 34.0, 32.7, 30.3, 30.3, 29.1, 29.0, 28.9, 28.5, 27.9, 23.0 (J_{CP} = 51.3), 22.5 (J_{CP} = 4.4), 21.7.

To a mixture of HU (0.19 g, 2.4 mmol) and potassium carbonate (68 mg, 0.5 mmol) in DMF (4 mL) was added Mito_{triMe}-Br (0.3 g, 0.5 mmol). The mixture was stirred at 45°C for 4 hr. Then, 100 mL of CH₂Cl₂ was added to the mixture. The organic layer was washed by 2 × 35 mL of H₂O. The organic layer was dried over sodium sulfate (Na₂SO₄), and the solvent was removed under reduced pressure. Then, Et₂O was added to the mixture to precipitate the compound. Purification by preparative high-performance liquid chromatography (HPLC) on C18 column (H₂O/CH₃CN containing 0.1% TFA as a gradient) was performed to deliver the corresponding Mito₁₀-HU_{triMe} (0.18 g, 57% yield).

HRMS calculated for Mito₁₀-HU_{triMe} C₃₂H₄₄N₂O₂P⁺ [M]⁺ 519.3135, found, 519.3134.

³¹P NMR (400.13 MHz, CD₃CN) δ 22.58. ¹H NMR (400.13 MHz, CD₃CN) δ 7.60-7.53 (12H, m), 3.78 (2H, t, J = 6.7), 3.12-3.05 (2H, m), 2.5 (9H, s), 1.66-1.20 (16H, m). ¹³C NMR (75 MHz, CD₃CN) δ 162.2, 160.7, 160.4, 160.0, 159.7, 147.1, 134.1, 133.9, 131.5, 131.4, 117.9, 116.4, 115.5, 77.0, 33.7, 33.6, 29.6, 29.4, 28.9, 28.4, 26.1, 22.5 (d, J = 52.1), 22.6 (d, J = 4.4), 21.4 (d, J = 1.5).

Synthesis of 4-[(carbamoylamino)oxy]-butyltriphenylphosphonium trifluoroacetate (Mito₄-HU). To a mixture of HU (0.8 g, 10 mmol) and potassium carbonate (0.28 g, 2 mmol) in DMF (4 mL) was added (4-bromobutyl)-triphenylphosphonium bromide (1 g, 2 mmol). The mixture was stirred at 45°C for 4 hr. 100 mL of CH₂Cl₂ was then added to the mixture. The organic layer was washed by 2 × 35 mL of H₂O. The aqueous layer is saturated in sodium chloride (NaCl) and extracted by 100 mL of chloroform (CHCl₃). The organic layer was dried over Na₂SO₄, and the solvent was removed under reduced pressure. Et₂O was then added to the mixture to precipitate the compound. Purification on C18 column (H₂O/CH₃CN containing 0.1% TFA as a gradient) was performed to deliver the corresponding Mito₄-HU (0.47 g, 48% yield).

HRMS calculated for Mito₄-HU C₂₃H₂₆N₂O₂P⁺ [M]⁺ 393.1726, found, 393.1728.

³¹P NMR (400.13 MHz, (CD₃)₂SO) δ 23.93. ¹H NMR (400.13 MHz, (CD₃)₂SO) δ 7.97-7.69 (15H, m), 6.31 (2H, s), 3.78-3.68 (4H, m), 1.86-1.76 (2H, m), 1.68-1.57 (2H, m). ¹³C NMR (75 MHz, (CD₃)₂SO) δ 160.9, 135.0, 134.8, 133.8, 133.7, 133.6, 133.5, 130.4, 130.3, 130.2, 119.0, 118.2, 74.1, 28.1 (d, J = 16.9), 20.2 (d, J = 49.9), 18.8 (d, J = 2.9).

Synthesis of 10-[(carbamoylamino)oxy]-decyltriphenylphosphonium trifluoroacetate (Mito₁₀-HU). To a mixture of HU (0.4 g, 5.0 mmol) and potassium carbonate (0.13 g, 0.9 mmol) in DMF (4 mL) was added (10-bromodecyl)-triphenylphosphonium bromide (Pan et al., 2018) (0.5 g, 0.9 mmol). The mixture was stirred at 45°C for 4 hr. 100 mL of CH₂Cl₂ was then added to the mixture. The organic layer was washed by 2 × 35 mL of H₂O. The organic layer was dried over Na₂SO₄ and the solvent was removed under reduced pressure. Et₂O was then added to the mixture to precipitate the compound. Purification by preparative HPLC on C18 column (H₂O/CH₃CN containing 0.1% TFA as a gradient) was performed to deliver the corresponding Mito₁₀-HU (0.22 g, 44% yield).

HRMS calculated for Mito₁₀-HU C₂₉H₃₈N₂O₂P⁺ [M]⁺ 477.2665, found, 477.2667.

^{31}P NMR (400.13 MHz, CDCl_3) δ 24.06. ^1H NMR (400.13 MHz, CDCl_3), δ 7.86-7.60 (15H, m), 3.81 (2H, t, $J = 6.5$), 3.35-3.19 (2H, m), 1.70-1.40 (6H, m), 1.36-1.11 (10H, m). ^{13}C NMR (75 MHz, CDCl_3) δ 160.7, 160.3, 135.3, 135.2, 133.3, 133.2, 130.7, 130.5, 118.5, 117.4, 76.8, 30.4, 30.2, 29.0, 28.9, 28.8, 28.6, 27.8, 25.6, 22.4 (d, $J = 50.1$), 22.4 (d, $J = 4.4$).

Synthesis of 12-[(carbamoylamino)oxy]-dodecyltriphenylphosphonium trifluoroacetate (Mito₁₂-HU). To a mixture of HU (0.35 g, 4.60 mmol) and potassium carbonate (0.13 g, 0.9 mmol) in DMF (3 mL) was added (12-bromododecyl)-triphenylphosphonium bromide (Cheng et al., 2020a) (0.5 g, 0.85 mmol). The mixture was stirred at 45°C for 4 hr. 100 mL of CH_2Cl_2 was then added to the mixture. The organic layer was washed by 2 × 35 mL of H_2O . The organic layer was dried over Na_2SO_4 and the solvent was removed under reduced pressure. Et_2O was then added to the mixture to precipitate the compound. Purification by low-pressure chromatography on C18 column ($\text{H}_2\text{O}/\text{CH}_3\text{CN}$ containing 0.1% TFA as a gradient) was performed to deliver the corresponding Mito₁₂-HU (0.2 g, 38% yield).

HRMS calculated for Mito₁₂-HU $\text{C}_{31}\text{H}_{42}\text{N}_2\text{O}_2\text{P}^+$ [M]⁺ 505.2978, found, 505.2980.

^{31}P NMR (400.13 MHz, $(\text{CD}_3)_2\text{SO}$) δ 24.06. ^1H NMR (400.13 MHz, $(\text{CD}_3)_2\text{SO}$), δ 7.91-7.73 (15H, m), 3.65 (2H, t, $J = 6.9$), 3.61-3.49 (2H, m), 1.59-1.39 (6H, m), 1.33-1.14 (14H, m). ^{13}C NMR (75 MHz, $(\text{CD}_3)_2\text{SO}$) δ 160.9, 134.9, 134.8, 133.7, 133.5, 133.4, 133.3, 130.3, 130.2, 130.1, 119.0, 118.2, 75.4, 28.9, 28.1, 28.7, 27.6, 21.7 (d, $J = 4.4$), 20.2 (d, $J = 49.9$).

Synthesis of 14-[(carbamoylamino)oxy]-tetradecyltriphenylphosphonium trifluoroacetate (Mito₁₄-HU). Aqueous hydrogen bromide (48%, 70 mL, 4.2 mmol) was added dropwise to acetic anhydride (120 mL, 1.27 mol) at 0°C. To this solution, 14-hydroxytetradecanol (5 g, 0.02 mol) was added and the mixture was brought to reflux for 24 hr. Then, the dihalide was extracted with pentane and washed with an excess of H_2O (5 × 50 mL) and sodium bicarbonate (50 mL). The organic layer was dried over Na_2SO_4 . The solvent was removed under reduced pressure. 1,14-dibromotetradecane was obtained in quantitative yield.

1,14-Dibromotetradecane: ^1H NMR (400.13 MHz, CDCl_3) δ 3.41 (t, 4H, $J = 6.9$), 1.86 (quint., 4H, $J = 6.9$, 14.1), 1.49-1.37 (4H, m), 1.36-1.24 (16H, m).

A mixture of 1,14-dibromotetradecane (6.7 g, 0.018 mol) and triphenylphosphine (1 g, 3.8 mmol) was stirred at 90°C for 6 hr. The resulting mixture was washed with Et_2O . Purification by flash chromatography using pentane, Et_2O , and $\text{CH}_2\text{Cl}_2/\text{EtOH}$ (9/1) successively delivered the corresponding Mito₁₄-Br (1.9 g, 80% yield).

(14-Bromotetradecyl)-triphenylphosphonium (Mito₁₄-Br): ^{31}P NMR (400.13 MHz, CDCl_3) δ 24.54. ^1H NMR (400.13 MHz, CDCl_3), δ 7.94-7.63 (15H, m), 3.90-3.78 (2H, m), 3.40 (t, 2H, $J = 6.9$), 1.85 (quint., 2H, $J = 7.0$, 14.0), 1.66-1.57 (4H, m), 1.46-1.37 (2H, m), 1.30-1.14 (16H, m). ^{13}C NMR (75 MHz, CDCl_3) δ 134.9, 134.8, 133.5, 133.4, 130.4, 130.3, 118.5, 117.7, 33.4, 32.6, 30.3, 30.1, 29.3, 29.2, 29.1, 28.9, 28.5, 27.9, 22.9, 22.5, 22.4.

To a mixture of HU (0.4 g, 5.2 mmol) and potassium carbonate (0.13 g, 0.9 mmol) in DMF (3 mL) was added (14-bromotetradecyl)-triphenylphosphonium bromide, (0.5 g, 0.85 mmol). The mixture was stirred at 45°C for 4 hr. 100 mL of CH_2Cl_2 was then added to the mixture. The organic layer was washed by 2 × 35 mL of H_2O . The organic layer was dried over Na_2SO_4 and the solvent was removed under reduced pressure. Et_2O was then added to the mixture to precipitate the compound. Purification by low-pressure chromatography on C18 column ($\text{H}_2\text{O}/\text{CH}_3\text{CN}$ containing 0.1% TFA as a gradient) was performed to deliver the corresponding Mito₁₄-HU (0.23 g, 46% yield).

HRMS calculated for Mito₁₄-HU $\text{C}_{33}\text{H}_{46}\text{N}_2\text{O}_2\text{P}^+$ [M]⁺ 533.3291, found, 533.3290.

^{31}P NMR (400.13 MHz, CD_3CN) δ 23.63. ^1H NMR (400.13 MHz, CD_3CN), δ 7.92-7.63 (15H, m), 5.71-5.23 (2H, m), 3.76 (2H, t, $J = 6.9$), 3.21-3.10 (2H, m), 1.68-1.56 (4H, m), 1.52-1.42 (2H, m), 1.38-1.18 (18H, m). ^{13}C NMR (75 MHz, CD_3CN) δ 136.2, 136.1, 134.7, 133.6, 131.4, 131.3, 119.9, 119.1, 118.4, 77.4, 31.2, 31.1, 30.4, 30.33, 30.32, 30.2, 29.9, 29.4, 28.9, 26.7, 23.0 (d, $J = 4.4$), 22.7 (d, $J = 51.3$).

Synthesis of 16-[(carbamoylamino)oxy]-hexadecyltriphenylphosphonium trifluoroacetate (Mito₁₆-HU). Aqueous hydrogen bromide (48%, 70 mL, 4.2 mmol) was added dropwise to acetic anhydride (120 mL, 1.27 mol) at 0°C. To this solution, 16-hydroxyhexadecanol (5 g, 0.02 mol) was added and the mixture was brought to reflux for 24 hr. The dihalide was then extracted with pentane and washed with excess of H₂O (5 × 50 mL) and sodium bicarbonate (50 mL). The organic layer was dried over Na₂SO₄. The solvent was removed under reduced pressure. 1,16-dibromohexadecane was obtained in quantitative yield.

1,16-Dibromohexadecane: ¹H NMR (400.13 MHz, CDCl₃) δ 3.41 (4H, t, J = 6.8), 1.86 (4H, quint., J = 7.0, 14.0), 1.48-1.38 (4H, m), 1.35-1.25 (20H, m).

A mixture of 1,16-dibromohexadecane (6 g, 15 mmol) and triphenylphosphine (1 g, 3.8 mmol) was stirred at 90°C for 6 hr. The resulting mixture was washed with Et₂O. Purification by flash chromatography using pentane, Et₂O, and CH₂Cl₂/EtOH (9/1) as eluents successively delivered the corresponding (16-Bromohexadecyl)-triphenylphosphonium, Mito₁₆-Br (1.3 g, 53 % yield).

HRMS calculated for Mito₁₆-Br C₃₄H₄₇BrP⁺ [M]⁺ 565.2593, found, 565.2593.

(16-Bromohexadecyl)-triphenylphosphonium (Mito₁₆-Br): ³¹P NMR (400.13 MHz, CDCl₃) δ 24.29. ¹H NMR (400.13 MHz, CDCl₃) δ 7.87-7.64 (15H, m), 3.76-3.65 (2H, m), 3.37 (2H, t, J = 6.9), 1.86-1.75 (2H, m), 1.65-1.54 (4H, m), 1.43-1.31 (2H, m), 1.32-1.12 (20H, m). ¹³C NMR (75 MHz, CDCl₃) δ 134.94, 134.91, 133.6, 133.5, 130.4, 130.3, 118.7, 117.8, 33.9, 32.7, 30.4, 30.2, 29.4, 29.3, 29.2, 29.0, 28.6, 28.0, 22.8 (d, J = 49.9), 22.5 (d, J = 4.4).

To a mixture of HU (0.2 g, 2.6 mmol) and potassium carbonate (66 mg, 0.48 mmol) in DMF (3 mL) was added (16-bromohexadecyl)-triphenylphosphonium bromide (0.31 g, 0.48 mmol). The mixture was stirred at 45°C for 4 hr. 100 mL of CH₂Cl₂ was then added to the mixture. The organic layer was washed by 2 × 35 mL of H₂O. The organic layer was dried over Na₂SO₄ and the solvent was removed under reduced pressure. Et₂O was then added to the mixture to precipitate the compound. Purification by low-pressure chromatography on C18 column (H₂O/CH₃CN containing 0.1% TFA as a gradient) was performed to deliver the corresponding Mito₁₆-HU (0.27 g, 82% yield).

HRMS calculated for Mito₁₆-HU C₃₅H₅₀N₂O₂P⁺ [M]⁺ 561.3604, found, 561.3611.

³¹P NMR (400.13 MHz, CD₃CN) δ 23.67. ¹H NMR (400.13 MHz, CD₃CN) δ 7.92-7.82 (3H, m), 7.75-7.68 (12H, m), 5.75-5.35 (2H, m), 3.75 (2H, t, J = 6.6), 3.23-3.14 (2H, m), 1.68-1.55 (4H, m), 1.53-1.44 (2H, m), 1.36-1.19 (22H, m). ¹³C NMR (75 MHz, CD₃CN) δ 61.7, 160.7, 160.0, 159.6, 136.2, 136.1, 134.8, 133.7, 131.4, 131.3, 119.9, 119.1, 118.4, 77.3, 31.2, 31.1, 30.42, 30.40, 30.37, 30.35, 30.34, 30.2, 29.9, 29.4, 28.9, 26.7, 23.0 (d, J = 4.4), 22.7 (d, J = 51.4).

Synthesis of 20-[(carbamoylamino)oxy]-eicosanyltriphenylphosphonium trifluoroacetate (Mito₂₀-HU). 20-Hydroxyeicosanol was obtained by adapting the procedures from Chanda et al. (Chanda and Ramakrishnan, 2015).

Aqueous hydrobromic acid (48%, 70 mL, 4.2 mmol) was added dropwise to acetic anhydride (120 mL, 1.27 mol) at 0°C. To this solution, 20-hydroxyeicosanol (6 g, 0.02 mol) was added and the mixture was brought to reflux for 24 hr. Then, the dihalide was extracted with pentane (500 mL) and washed with excess of H₂O (5 × 100 mL) and saturated solution of sodium bicarbonate (2 × 100 mL). The organic layer was dried over sodium sulfate. The solvent was removed under reduced pressure. 1,20-dibromoeicosane was obtained in 89% yield (7.5 g).

A mixture of 1,20-dibromoeicosane (6.6 g, 15 mmol) and triphenylphosphine (1 g, 3.8 mmol) was stirred at 90°C for 12 hr. The resulting mixture was washed with Et₂O. Purification by flash chromatography using pentane, Et₂O, and CH₂Cl₂/EtOH (9/1) as eluents successively delivered the corresponding (20-bromoeicosanyl)-triphenylphosphonium bromide, Mito-Br-C₂₀ (1.5 g, 56 % yield).

ESI-MS for Mito-Br-C₂₀ C₃₈H₅₅BrP⁺ [M]⁺ 624.4.

To a mixture of HU (0.35 g, 4.6 mmol) and potassium carbonate (0.13 g, 0.94 mmol) in DMF (3 mL) was added (20-bromoeicosanyl)-triphenylphosphonium bromide, (0.50 g, 0.71 mmol). The mixture was stirred at 45°C for 4 hr. Then, 100 mL of CH₂Cl₂ was added to the mixture. The organic layer was washed by 2 × 35 mL of H₂O. The organic layer was dried over Na₂SO₄ and the solvent was removed under reduced pressure. Then, sodium sulfate was added to the mixture to precipitate the compound. Purification by C18 column (using H₂O/MeCN [9/1 to 100%] containing 0.1% TFA) was performed to deliver the corresponding Mito₂₀-HU (0.26 g, 50% yield).

HRMS calculated for Mito₂₀-HU C₃₉H₅₈N₂O₂P⁺ [M]⁺ 617.4230, found, 617.4231.

³¹P NMR (400.13 MHz, CDCl₃) δ 23.61. ¹H NMR (400.13 MHz, CDCl₃) δ 7.83-7.76 (3H, m), 7.72-7.65 (12H, m), 3.81 (2H, t, J = 6.7), 3.37-3.26 (2H, m), 1.66-1.56 (4H, m), 1.56-1.48 (2H, m), 1.30-1.15 (30H, m). ¹³C NMR (75 MHz, CD₃CN) δ 162.4, 160.9, 160.5, 136.2, 136.1, 134.7, 133.6, 131.4, 131.3, 119.9, 119.1, 118.5, 77.4, 31.2, 31.0, 30.5, 30.4, 30.39, 30.35, 30.24, 30.23, 29.9, 29.4, 28.9, 26.7, 23.0 (d, J = 4.4), 22.7 (d, J = 50.6).

Synthesis of decyloxyurea(Decyl-HU). To a mixture of HU (1.7 g, 22.3 mmol) and potassium carbonate (0.62 g, 4.5 mmol) in DMF (4 mL) was added bromodecane (1 g, 4.5 mmol). The mixture was stirred at 45°C for 4 hr. 100 mL of CH₂Cl₂ was then added to the mixture. The organic layer was washed by 2 × 35 mL of H₂O. The organic layer was dried over Na₂SO₄ and the solvent removed under reduced pressure. Et₂O was then added to the mixture to precipitate the corresponding to decyl-HU (0.3 g, 31% yield).

HRMS calculated for decyl-HU C₁₁H₂₄N₂O₂ [MH]⁺ 217.1911, found, 217.1911.

¹H NMR (400.13 MHz, (CD₃)₂SO), δ¹H NMR (400.13 MHz, (CD₃)₂SO), δ 6.23 (2H, s), 3.64 (2H, t, J = 6.5), 1.60-1.46 (2H, m), 1.34-1.17 (14H, m), 0.85 (3H, t, 6.7). ¹³C NMR (75 MHz, CDCl₃) δ 0.8, 75.4, 31.3, 28.95, 28.90, 28.8, 27.6, 25.3, 22.1, 13.9, 13.8.

Cell proliferation measurements

The IncuCyte Live-Cell Analysis system (Essen Bioscience Inc., Ann Arbor, MI) was used to monitor cell proliferation (Cheng et al., 2013, 2016; Boyle et al., 2018). As shown in previous publications (Cheng et al., 2013, 2016), this imaging system is probe-free and noninvasive, and enables continuous monitoring of cell confluence over several days. The increase in the percentage of cell confluence was used as a surrogate marker of cell proliferation. In a 96-well plate, cells were plated at 1,000 cells per well in triplicates and left to adhere overnight. Cells were then treated with HU and Mito-HUs, and the cell confluency was recorded over several days in the IncuCyte Live-Cell Analysis system.

Cytotoxicity assay

To determine the cytotoxicity of Mito-HUs, we used the SYTOX Green-based assay (Cheng et al., 2012). HCT116 cells were treated for up to 48 hr, and dead cells were monitored in real time in the presence of 200 nM SYTOX Green (Invitrogen, Carlsbad, CA) under an atmosphere of 5% CO₂:95% air at 37°C. Cells were then permeabilized with digitonin (120 μM) in the presence of SYTOX Green to determine the total cell number.

Mitochondrial oxygen consumption measurements

Mitochondrial oxygen consumption was measured using the Seahorse XF-96 Extracellular Flux Analyzer (Agilent, North Billerica, MA) (Cheng et al., 2013, 2016; Boyle et al., 2018; Weinberg and Chandel, 2015). After cells were treated with HU or Mito-HUs for 24 hr, the OCR-based assessment of mitochondrial complex activities was carried out on acutely permeabilized cells in the presence of different mitochondrial substrates, i.e., pyruvate/malate for complex I and duroquinol for complex III (Cheng et al., 2016, 2019; Salabei et al., 2014; Wheaton et al., 2014). Rotenone, malonate, and antimycin A (Sigma-Aldrich, St. Louis, MO) were used as specific inhibitors of mitochondrial complexes I, II, and III, respectively. Briefly, cells that were intact after treatments were immediately permeabilized using the Seahorse XF Plasma Membrane Permeabilizer (Agilent). The mitochondrial complex I-induced OCR was assayed in mannitol and sucrose buffer (Salabei et al., 2014) containing 10 mM pyruvate and 1.5 mM malate (substrates for complex I) and 10 mM malonate (which inhibits complex II activities). The mitochondrial complex III-driven OCR was assayed in a mannitol and sucrose buffer containing 0.5 mM duroquinol (substrate for complex III).

as well as 1 μ M rotenone and 10 mM malonate (which inhibit both complex I and II activities). The IC₅₀ values were determined as previously reported (Cheng et al., 2019).

Immunoregulatory measurements

To differentiate CD4⁺ T cells into a T_{reg} phenotype, splenocytes from SMARTA triple-reporter mice were processed and the red blood cells were lysed using an ACK (ammonium-chloride-potassium) lysis buffer. The cells were then activated with 1 μ g/mL GP₆₁₋₈₀ peptide (GenScript, Piscataway, NJ) and 5 ng/mL TGF- β 1 (Shenandoah Biotechnology, Inc., Warwick, PA). After one day of initial skewing, 100 μ g/mL IL-2 along with HU or Mito-HUs (n = 4–20) of varying concentrations were added to the culture. Cells were cultured for six days and split once cells reached confluency; cells were replenished with IL-2 and compound (*i.e.*, Mito-HUs) accordingly. After six days in culture, cells were stained to assess the viability and phenotypic analysis via flow cytometry. LIVE/DEAD fixable violet or aqua dead cell stain (Invitrogen) was used to assess cell viability. Only live cells were gated out for further functional analysis by using a fixable LIVE/DEAD stain. First, total population of cells was gated (FSC-A vs SSC-A). Then, single cells were gated (SSC-W vs SSC-H). Within the single cell population, we gated on the live CD4 T cells using a fixable Live/Dead stain (CD4 vs DEAD). Within the live CD4 T cells, we gated on CD25⁺FOXP3⁺ T_{regs} (FOXP3 vs CD25), as well as IFN γ -YFP⁺ CD4 T cells (IFN γ -YFP vs CD4).

The following antibodies were used for flow cytometry staining: APC-Cy7 anti-mouse CD4 (clone: GK1.5; BioLegend, San Diego, CA), APC anti-mouse CD25 (clone: PC61; BioLegend), and PE anti-mouse FOXP3 (clone: FJK-16S; eBioscience, San Diego, CA). Flow cytometry data were acquired using a BD Celesta flow cytometer (BD Biosciences, San Jose, CA) flow cytometer and analyzed using FlowJo (Treestar, Inc., Ashland, OR) (FlowJo Software, 2019).

MDSCs were generated from bone marrow cells isolated from C57bl/6 mice and cultured at a density of 1×10^6 cells/ml in RPMI with 10% fetal bovine serum and 25 ng/ml recombinant mouse GM-CSF (Shenandoah Biotechnology, Inc.) and 25 ng/ml recombinant mouse IL-6 (Shenandoah Biotechnology, Inc.) for three days. Then, cells were re-cultured in fresh media with inhibitors for an additional three days. Cells were scraped and examined by flow cytometry using the following markers: FITC-anti Ly6C (Biolegend, San Diego, CA), PE-Cy7 anti F4/80 (Biolegend), APC-Cy7 anti Ly6G (Biolegend), and Pacific Blue anti-CD11b (Biolegend). A gating strategy similar to that employed for the T cells was used in all MDSC differentiation assays, which were tested only on live cells after treatments. Flow cytometry data were acquired using a BD Celesta flow cytometer (BD Biosciences), and data were analyzed using FlowJo software (Treestar, Inc.).

QUANTIFICATION AND STATISTICAL ANALYSIS

Comparisons between the control group and treatment group were made using an unpaired Student's t-test analysis. *p* values of less than 0.05 were considered to be statistically significant. All values provided represent mean \pm standard deviation. The numbers of replicates per treatment group are shown as *n*. IC₅₀ values and fitting curves were calculated using OriginPro 2016 (OriginLab Corporation, Northampton, MA).